

1 **Bowen ratio-constrained global dataset of bulk air-sea turbulent**
2 **heat fluxes from 1993 to 2017**

3 Yizhe Wang^{a, b}, Ronglin Tang^{a, b, *}, Meng Liu^c, Lingxiao Huang^{a, b}, Zhao-Liang Li^{a, b, c}

4 ^a State Key Laboratory of Resources and Environment Information System, Institute of
5 Geographic Sciences and Natural Resources Research, Chinese Academy of Sciences,
6 Beijing 100101, China

7 ^b University of Chinese Academy of Sciences, Beijing 100049, China

8 ^c State Key Laboratory of Efficient Utilization of Arable Land in China, Institute of
9 Agricultural Resources and Regional Planning, Chinese Academy of Agricultural
10 Sciences, Beijing 100081, China

11 * Authors to whom correspondence should be addressed: tangrl@reis.ac.cn

12

13

14

15 **Abstract**

16 Air-sea turbulent heat fluxes, including the sensible heat flux (SHF) and latent heat
17 flux (LHF), along with the Bowen ratio (β , ratio of SHF to LHF), are crucial for
18 understanding air-sea interaction and global energy and water budgets. However, the
19 existing products, primarily developed using the semi-empirical bulk aerodynamic
20 methods and data-driven machine learning approaches, are often weak in accuracy and
21 physical rationality, due to the uncertainties in the environmental forcings and
22 inappropriate parameterizations. In this study, we generated a global daily 0.25° product
23 of bulk air-sea turbulent heat fluxes using the Bowen ratio-constrained Neural Network
24 (NN) model (referred to as the BrTHF model) that could coordinately estimate the SHF
25 and LHF, along with the observations from 197 globally distributed buoys and multi-
26 source remote sensing and reanalysis inputs. The spatial ten-fold cross-validation
27 results showed that the BrTHF model, achieving root mean square errors of 6.05 W/m^2 ,
28 23.67 W/m^2 and 0.22 and correlation coefficients of 0.93 , 0.91 and 0.25 for the SHF,
29 LHF and β , respectively, outperformed the physics-agnostic NN model and seven
30 widely used air-sea turbulent heat flux products (including JOFURO3, IFREMER,
31 SeaFlux, ERA5, MERRA2, OAFflux, and OHF). Furthermore, the inter-comparison of
32 the spatial distribution of multi-year means, as well as intra-annual and inter-annual
33 change patterns showed that the BrTHF product reliably simulated global SHF, LHF
34 and β , in contrast to the machine learning-based OHF product that failed to replicate
35 these patterns. The main advantage of the BrTHF model lies in its improved rationality
36 of β estimates, successfully eliminating the outliers observed in the physics-agnostic
37 NN model and the seven typical products. The improved SHF, LHF, and β estimates
38 can allow for more accurate quantification of the global air-sea energy and water
39 budgets, enhance our understanding of air-sea interaction, and improve projections of
40 climate change under global warming. The 0.25° daily global product from 1993 to
41 2017 can be freely accessed from the National Tibetan Plateau Data Center (TPDC)
42 [<https://doi.org/10.11888/Atmos.tpdc.302578>, Tang and Wang (2025)].

43 **Keywords:** Air-sea turbulent heat fluxes; Sensible heat flux; Latent heat flux; Bowen
44 ratio

45 **1. Introduction**

46 Air-sea turbulent heat fluxes, comprising the latent heat flux (LHF) and sensible
47 heat flux (SHF), play vital roles in the Earth's climate system by characterizing the
48 exchange of energy and water between the ocean and atmosphere (Wild et al., 2014;
49 Loeb et al., 2021; Fasullo et al., 2014). Accurate estimation of SHF, LHF and their
50 ratio—the Bowen ratio ($\beta = \text{SHF}/\text{LHF}$) is an essential prerequisite for advancing our
51 understanding of atmosphere-sea interaction (Gentemann et al., 2020), improving the
52 quantification of global water and energy budget (Zhang, 2023), and enhancing the
53 predictability of extreme weather events (Yu, 2019).

54 To estimate global air-sea turbulent heat fluxes, the semi-empirical bulk
55 aerodynamic method was developed based on the Monin-Obukhov similarity theory
56 (Monin and Obukhov, 1954). It establishes scaling relationships between fluxes and
57 near-surface meteorological variables such as wind speed, humidity, and temperature
58 (Yu, 2019). This method, for its ease of application, has been applied to generate tens
59 of widely used products in the past few decades (Shie et al., 2009; Liman et al., 2018;
60 Yu and Weller, 2007; Berry and Kent, 2011; Tomita et al., 2018; Crespo et al., 2019).
61 However, there were huge discrepancies in the global and regional magnitude and
62 patterns of SHF and LHF among these products, which seriously impeded our
63 understanding of ~~the key process of~~ the air-sea interaction and the global budget of
64 water and energy (Bentamy et al., 2017; Tang et al., 2024; Yu, 2019). The discrepancies
65 could be partly attributed to the substantial uncertainties in the environmental forcings
66 used to develop these products (Robertson et al., 2020) and the inappropriate
67 parameterizations (Brodeau et al., 2017; Jiang et al., 2024a; Jiang et al., 2024b; Yang et
68 al., 2024). More explicitly, existing parameterizations often rely on simplified
69 assumptions about atmospheric stability and boundary layer dynamics, which may not
70 hold under diverse environmental conditions. For instance, most bulk algorithms are

71 optimized for moderate wind regimes, resulting in degraded performance and increased
72 uncertainty when applied under weak wind regimes (Jiang et al., 2024a; Brunke, 2002).
73 At very high wind speeds, however, observations show that the drag coefficient can
74 decrease due to sea spray and whitecap formation, reducing effective surface roughness
75 and potentially biasing flux estimates (Cai et al., 2025). In addition, simplifications in
76 the treatment of sea surface skin temperature, saturation humidity, and air density in the
77 parameterizations can also introduce substantial uncertainty (Brodeau et al., 2017).
78 Together, these limitations can contribute a lot to the biases in the SHF and LHF
79 estimates which can even lead to the unphysical estimations of β , as Wang et al. (2024)
80 reported. To better describe and comprehend the air-sea interaction and the energy and
81 water budgets, the existing mode to produce global air-sea turbulent heat fluxes needs
82 improvement urgently.

83 Machine learning techniques have been extensively applied to upscale point-scale
84 in-situ measurements of a single variable (such as soil moisture, roughness, or
85 temperature) into grid-scale global datasets (Wang et al., 2023; Peng et al., 2022; O and
86 Orth, 2021; Nelson et al., 2024; Fu et al., 2023). These efforts highlight the great
87 potential of machine learning for more accurate and consistent multivariate coordinated
88 mapping (Karniadakis et al., 2021; Kashinath et al., 2021; Van Der Westhuizen et al.,
89 2023; Wang et al., 2024). However, the application of machine learning in global
90 mapping of air-sea turbulent heat fluxes remains limited. Among these studies, some
91 have focused on solely improving the accuracy of LHF, while the remaining studies
92 have mostly considered independent modeling of SHF and LHF (Bourras et al., 2007;
93 Cummins et al., 2024; Cummins et al., 2023; Zhou et al., 2024). In both
94 [approaches](#), however, most studies have not produced long-term flux products.
95 The only publicly available machine learning-based global air-sea turbulent heat fluxes
96 product, released by the National Oceanic and Atmospheric Administration (NOAA)
97 Ocean heat flux CDR (hereafter dubbed OHF), simultaneously modeled SHF and LHF
98 using a Neural Network (NN) technique (Clayson and Brown, 2016). Although it

99 performed well when validated against the observations from the tropical buoys, it
100 failed to capture the regional characteristics, particularly in areas where air-sea
101 turbulent heat exchange is intense (e.g. oceans with latitudes beyond 45° for SHF and
102 subtropical highs for LHF) (Tang et al., 2024). Additionally, it exhibited different
103 patterns of temporal evolution of global annual mean and opposite inter-annual trends
104 at both regional and global scales to most widely-used physical model-based products,
105 likely due to unreasonable construction of observation datasets [with data before and
106 after 2007 coming from SeaFlux in-situ datasets and ICOADS (International
107 Comprehensive Ocean-Atmosphere Data Set) datasets, respectively]. Furthermore, the
108 product likely suffers from unphysical estimates of the β due to neglecting the
109 interrelations among SHF, LHF and β during the model construction.

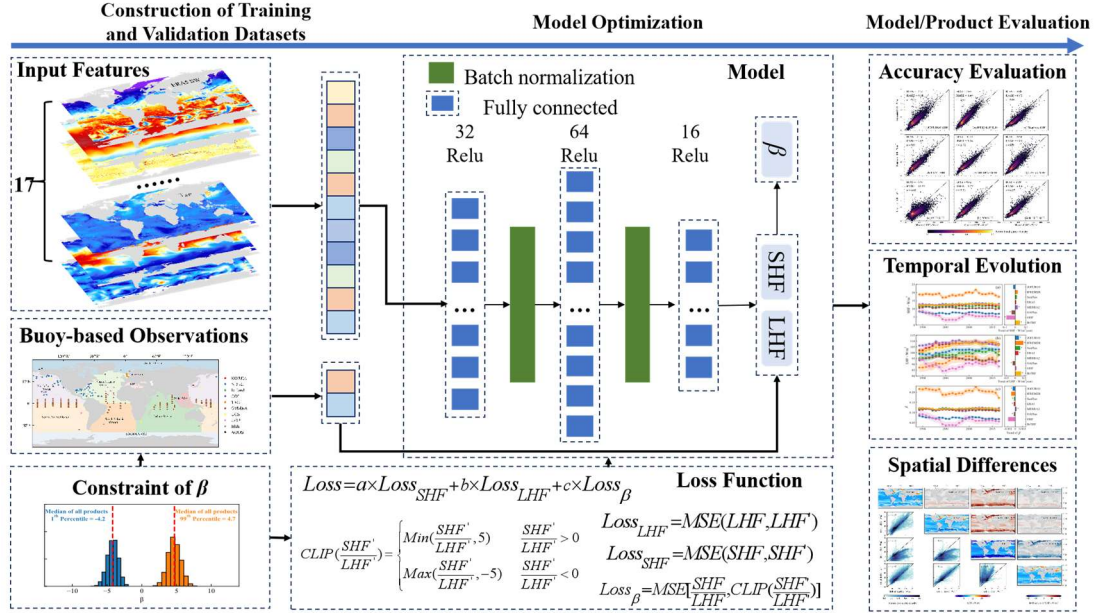
110 To improve the estimation of SHF, LHF, and β in a coordinative framework, we
111 recently proposed an innovative Bowen ratio-informed data-driven model by
112 considering the synergistic changes [on the one hand, ensuring physical consistency
113 (i.e., $\text{SHF}/\text{LHF} = \beta$); on the other hand, achieving high-accuracy estimations of SHF,
114 LHF, and β simultaneously] using a Random Forest (RF) technique (Wang et al., 2024).
115 Validation against hourly eddy covariance (EC) flux measurements from 53 historical
116 cruises demonstrated the model's superior performance, achieving high accuracy in
117 estimating SHF, LHF, and β , with results that are physically consistent. Wang et al.
118 (2024) highlights the feasibility of simultaneously estimating SHF, LHF, and β with
119 high accuracy using machine learning techniques, offering strong potential for global
120 mapping that aligns with physical consistency. However, since EC observations are
121 difficult to obtain at sea due to platform motion and airflow distortion (Bourras et al.,
122 2019; Bourras et al., 2009)—their limited spatio-temporal coverage constrains the
123 application of the model for global mapping. Buoy-based flux observations provide a
124 viable alternative. Buoy data offer globally representative flux samples with adequate
125 volume and acceptable accuracy, which have been widely used to evaluate the
126 performance of global products (Bentamy et al., 2017; Bourras, 2006; Tang et al., 2024;

127 Weller et al., 2022; Zhou et al., 2020) and support global modeling (Chen et al., 2020a)
128 and analysis (Song et al., 2024; Yan et al., 2024).

129 The primary objectives of this study are three fold: (1) to develop an innovative
130 Bowen ratio-constrained statistical model for improving the air-sea SHF, LHF and β
131 estimates (referred to as the BrTHF model hereafter) using the machine learning
132 technique and global buoy-based air-sea turbulent heat fluxes observations; (2) to
133 demonstrate the superiority of the statistical model through an inter-comparison with
134 seven widely used global products and the estimates from the physics-free machine
135 learning-based model; (3) to produce a global daily 0.25° dataset based on the BrTHF
136 model over ice-free oceans covering the period from 1993 to 2017. The flux
137 observations from 197 global distributed buoys, along with multi-source satellite-based
138 and reanalysis-based inputs, were collected to construct the models and further produce
139 the global air-sea turbulent heat fluxes dataset. The accuracy and spatio-temporal
140 patterns of the SHF, LHF and β estimates were inter-compared with seven widely used
141 products, including the remote sensing-based JOFURO v3, IFREMER v4.1 and
142 SeaFlux v3, as well as reanalysis-based ERA5 and MERRA2, hybrid-based OAFlex v3
143 and machine learning-based OHF v2 products.

144 **2. Data and Methods**

145 The following sub-sections provide an overview of the development of the BrTHF
146 product, detailing the construction of air-sea turbulent heat fluxes observation datasets,
147 learning datasets and the BrTHF model, as well as the evaluation strategies used in this
148 study, as indicated in Figure 1.



149

150 **Figure 1. flowchart of the generation of a global product of air-sea SHF, LHF and β by the**
 151 **BrTHF model**

152 **2.1 Air-sea turbulent heat fluxes observation datasets**

153 To obtain the buoy-derived air-sea turbulent heat fluxes observations, the hourly
 154 or sub-hourly oceanic and atmospheric measurements including sea surface
 155 temperature (T_s), sea surface air temperature (T_a), sea surface wind speed (WS) and
 156 relative humidity (RH) were firstly collected at 268 buoys covering a variety of ocean
 157 basins from 13 organizations or networks. Detailed information about the buoy sources
 158 and the number of buoys from each provider is summarized in Table 1.

159 **Table 1 Summary of f buoys used in this study**

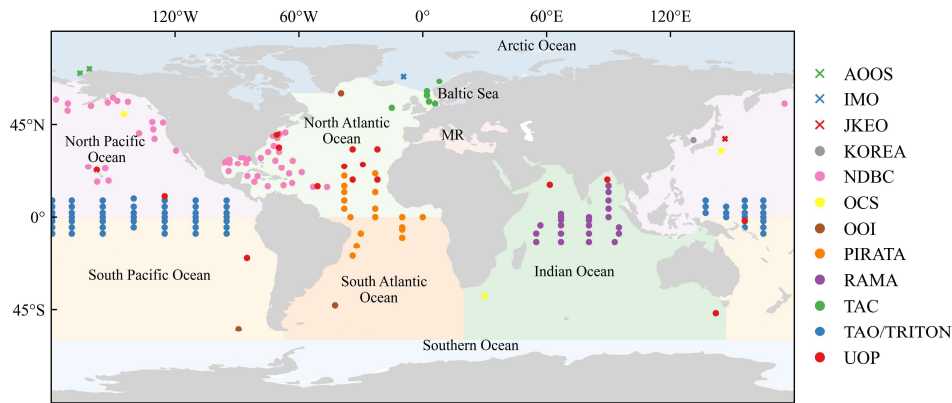
Network/Organization	Number of Buoys	Network/Organization	Number of Buoys
TAO/TRITON (Tropical Atmosphere Ocean / TRITON)	67	KOREA (Korea Meteorological Administration)	24
PIRATA (Prediction and Research Moored Array)	20	OOI (Ocean Observatories Initiative)	6
RAMA (Research Moored Array for Monsoon Analysis)	23	AOOS (Alaska Ocean Observing System)	2
NDBC (National Data Buoy Center)	73	JKEO (Japan Agency for Marine-Earth Science and Tech.)	1
Copernicus Marine In Situ TAC	19	Irish Weather Buoy Network	6
UOP (Upper Ocean Processes)	23	Icelandic Meteorological Office	1

160 For certain buoys lacking RH measurements [e.g. buoys from NDBC (National
 161 Data Buoy Center) provided dew point temperature (DEW) rather than RH], the RH
 162 was computed using DEW and T_a . To ensure the quality of the measurements, we
 163 filtered the records based on the quality control recommendations provided by the data
 164 providers. Further refinement was also made by removing the questionable values that
 165 exceeded three standard deviations (3σ) for each variable at individual buoys.

166 Once the data was cleaned, daily mean aggregation was applied to the oceanic and
 167 atmospheric measurements. Given the varying temporal resolutions of the
 168 measurements (e.g. NDBC provided hourly observations before 2005 and 10-min
 169 observations thereafter), we only retained the daily mean data when the fraction of the
 170 valid hourly or sub-hourly observations exceeded 80% on a given day.

171 After the above mentioned data preprocessing, the daily buoy-derived air-sea
 172 turbulent heat fluxes (SHF and LHF) observations were then calculated using the daily
 173 oceanic and atmospheric measurements combined with the version 3.5 of Coupled
 174 Ocean-Atmosphere Response Experiment (COARE3.5) model (Edson, 2013)
 175 (available at <https://github.com/NOAA-PSL/COARE-algorithm>) with the cool-skin
 176 and warm-layer calculation switched off. The configuration follows the practice
 177 adopted by Pacific Marine Environmental Laboratory for producing daily air-sea
 178 turbulent heat flux products
 179 (<https://www.pmel.noaa.gov/tao/drupal/flux/documentation-lw.html>) at Global
 180 Tropical Moored Buoy Array (TAO/TRITON, PIRATA, and RAMA). Although outliers
 181 of β exist in observations, some are likely caused by measurement errors. ss Note that
 182 outliers of β present in the observations are likely associated with uncertainties in the
 183 model-derived estimates and input data. —Considering that such outliers can severely
 184 impede model training and evaluation, it was necessary to constrain β within a
 185 reasonable range to enable simultaneous high-accuracy estimation of SHF, LHF, and β .

186 Therefore, following the air-sea turbulent heat fluxes computations, we further made a
 187 quality control on the derived SHF and LHF observations to exclude the abnormal
 188 records, by filtering the observations based on the range of daily β values determined
 189 from seven widely-used flux products. Specifically, we calculated the cumulative
 190 distribution of daily β for each product and their ensemble (across all products). The
 191 medians of the 1st and 99th percentiles, approximately -5 and 5, respectively, were
 192 selected as the minimum and maximum of valid daily β , as shown in Figure S1. In total,
 193 this study compiled 463,585 observations of valid daily air-sea turbulent heat flux from
 194 197 buoy stations (Figure 2 and Table S1) in the Arctic Ocean, Pacific Ocean, Atlantic
 195 Ocean and Indian Ocean.



196
 197 **Figure 2. Geographic locations of 197 buoy sites from 12 organizations or networks involved**
 198 **in this analysis including TAO/TRITON, PIRATA, RAMA, NDBC, TAC, UOP, OOI, AOOS,**
 199 **KOREA, OCS, JKEO and IMO. The boundaries of global land and open oceans were sourced**
 200 **from the Natural Earth dataset (<https://www.naturalearthdata.com/downloads/>) and the**
 201 **Global Oceans and Seas dataset (<https://www.marinerregions.org/sources.php>), respectively.**
 202 **Abbreviations MR refers to the Mediterranean Region. It should be noted that the Caspian**
 203 **Sea was not included within the boundaries of the open oceans and is shown in white.**

204 Finally, the quality-controlled observations were collected to train and validate the
 205 BrTHF model. Note that the COARE-based observations at the buoy stations have
 206 already widely applied as a benchmark for global air-sea turbulent heat flux product
 207 development and evaluation (Bentamy et al., 2017; Chen et al., 2020b; Tang et al., 2024;
 208 Weller et al., 2022)

209 2.2 Learning datasets and state-of-the-art products

210 2.2.1 Learning datasets for training the neural network

211 Learning variables were carefully selected based on their potential impacts on the
212 variations of the air-sea turbulent heat fluxes (Grist et al., 2016; Kudryavtsev et al.,
213 2014; Myslenkov et al., 2021; Song, 2020, 2021; Yan et al., 2024) to conduct the feature
214 selection (see section 2.3.1). These variables include T_a , sea surface air specific
215 humidity (Q_a), Mean Sea Level Pressure (SLP), Downward Long Wave Radiation Flux
216 (LW), Downward Short Wave Radiation Flux (SW), T_s , sea surface specific humidity
217 (Q_s), Absolute Dynamic Topography (ADT), Sea Level Anomaly (SLA), Sea Surface
218 Salinity (SSS), Sea Surface Density (SSD), Ocean Mixed Layer Current Velocity (CS),
219 WS , Significant Wave Height (SWH), Wave period (T_p), as well as gradient of
220 temperature ($diff_T$) calculated using the T_s and T_a , and gradient of humidity ($diff_Q$)
221 calculated using the Q_s and Q_a .

222 Datasets of these learning variables were collected from multiple publicly
223 available sources, as summarized in Table 2 and were used as the input features for
224 training the neural network. The Multi Observation Global Ocean Sea Surface Salinity
225 and Sea Surface Density (MOGOSD) dataset and Global Ocean Waves (GOW)
226 Reanalysis dataset were spatially resampled to a 0.25° resolution using mean
227 aggregation, while temporal mean aggregation to daily values was applied to the GOW
228 dataset (originally at 3-hour resolution) and Cross-Calibrated Multi-Platform (CCMP)
229 wind vector analysis dataset (6-hour resolution). Additionally, a daily ERA5 sea-ice
230 mask was applied to the datasets to mitigate the impact of sea ice.

231 2.2.2 State-of-the-art products for inter-comparison

232 Seven widely used air-sea turbulent heat fluxes products, involving remote
233 sensing-based JOFURO3, IFREMER and SeaFlux, as well as reanalysis-based ERA5
234 and MERRA2, hybrid-based OAFlex and machine learning-based OHF products were
235 selected for inter-comparison.

236 The remote sensing-based JOFURO3, IFREMER, and SeaFlux products were

237 developed by the Japanese Ocean Flux Data Sets under the Remote Sensing
238 Observations (J-OFURO) research project, the Institute Français de Recherche pour
239 l'Exploitation de la Mer (IFREMER), and the NASA Global Hydrology Resource
240 Center (GHRC) Distributed Active Archive Center (DAAC), respectively. The
241 reanalysis-based ERA5 and MERRA2 products were developed by the ECMWF and
242 NASA Global Modeling and Assimilation Office (GMAO), respectively. The hybrid-
243 based OAFlux and machine learning-based OHF products were developed or published
244 by the Woods Hole Oceanographic Institution (WHOI) and NOAA Ocean Surface
245 Bundle (OSB) Climate Data Record (CDR), respectively. With the exception of the
246 OHF product calculating SHF and LHF simultaneously using a NN model without a
247 constraint, all other products employed bulk aerodynamic methods to estimate SHF and
248 LHF. The JOFURO3, IFREMER, and OAFlux products used the COARE3.0 model,
249 while the SeaFlux used the COARE3.5 model. Differently, the ERA5 adopted the bulk
250 aerodynamic method used by the ECMWF, and the MERRA2 used the method by the
251 GEOS. These products provide SHF and LHF estimates at a 0.25° spatial resolution,
252 except for the MERRA2 ($0.5^\circ \times 0.625^\circ$) and OAFlux (1°). Additionally, most products
253 provide daily SHF and LHF estimates, while only the OHF product provides estimates
254 at a 3-hour interval. For further inter-comparison, the daily mean aggregation was
255 applied to the OHF products. More details about the seven products can be found in the
256 review of Tang et al. (2024).

Table 2 Summary of learning datasets used in this study

Dataset source	Resolution	Variables	Urls
ERA5	0.25°/daily	Sea surface air temperature (T_a), sea surface air specific humidity (Q_a), mean sea level pressure (SLP), downward long wave radiation flux (LN) and downward short wave radiation flux (SN)	https://cds.climate.copernicus.eu/datasets/derived-era5-single-levels-daily-statistics?tab=overview
OSCAR	0.25°/daily	Ocean mixed layer current velocity (CS)	https://podaac.jpl.nasa.gov/dataset/OSCAR_L4_OC_FINAL_V2.0
CCMP	0.25°/6-hour	Wind speed (WS)	https://data.remss.com/ccmp/v03.0/daily/
MOGOSD	0.125°/daily	Sea surface salinity (SSS) and sea surface density (SSD),	https://data.marine.copernicus.eu/product/MULTIOBS_GLO_PHY_S_SURFACE_MYNRT_015_013/description
SSH	0.25°/daily	Absolute dynamic topography (ADT) and sea level anomaly (SLA)	https://data.marine.copernicus.eu/product/SEALEVEL_GLO_PHY_CLIMATE_L4_MY_008_057/description
GOW	0.2°/3-hour	Significant wave height (SWH) and wave period (T_p)	https://data.marine.copernicus.eu/product/GLOBAL_MULTITYEAR_WAV_001_032/description
OISST	0.25°/daily	Sea surface temperature (T_s) and sea surface specific humidity (Q_s)	https://www.ncei.noaa.gov/data/sea-surface-temperature-optimum-interpolation/v2.1/access/avhrr/
OISST – ERA5	0.25°/daily	Gradient of temperature ($diff_T$) and gradient of humidity ($diff_Q$)	-

Table 3 Summary of the state-of-the-art air-sea turbulent heat fluxes products used for inter-comparison in this study

Dataset source	Resolution	Model	Variables	Urls
JOFURO3	0.25°/daily	COARE3.0		https://www.j-ofuro.com/en/
IFREMER	0.25°/daily	COARE3.0		ftp://ftp.ifremer.fr/ifremer/cersat/data/heat-flux/ifremer/v4.1/daily
SeaFlux	0.25°/daily	COARE3.5		https://www.earthdata.nasa.gov/data/catalog/glnc-daac-seaflux-1
MERRA2	0.5° × 0.625°/daily	GEOS	Latent heat flux (LHF), sensible heat flux (SHF) and Bowen ratio ($\beta =$ SHF/LHF)	https://developers.google.com/earth-engine/datasets/catalog/NASA_GSFC_MERRA_flux_2?hl=zh-cn#bands
ERA5	0.25°/daily	ECMWF	Bowen ratio ($\beta =$ SHF/LHF)	https://cds.climate.copernicus.eu/datasets/derived-era5-single-levels-daily-statistics?tab=overview
OAFflux	1°/daily	COARE3.0		ftp://ftp.whoi.edu/pub/science/oaf Flux/data_v3
OHF	0.25°/3-hour	Neural Network model		https://www.ncei.noaa.gov/products/climate-data-records/ocean-heat-fluxes

262 2.3 Construction of the BrTHF model

263 2.3.1 Feature selection

264 The study employed a random forest (RF) model to evaluate the importance scores
265 of 17 oceanic and atmospheric learning variables (with datasets collected in Section 2.2)
266 for target variables (SHF and LHF), aiming to filter out less influential variables. As
267 shown in Table S2, the variable importance assessment revealed that $diff_T$ and $diff_Q$
268 showed the highest importance score (71.56% and 49.93%) for SHF and LHF
269 modelling, respectively; additionally, WS exhibited the second highest importance for
270 both SHF (10.19%) and LHF (27.59%) modelling. Building upon the importance
271 evaluation and through careful screening of highly correlated variables, we ultimately
272 selected 11 key environmental features for subsequent air-sea turbulent heat fluxes
273 modelling including SLP , LW , SW , SSS , ADT , CS , WS , SWH , T_p , $diff_Q$, and $diff_T$.

274 2.3.1 Model construction and optimization

275 We selected the NN technique to build the BrTHF model due to its strong ability
276 to capture the complex nonlinear relationships between the multiple_-inputs and
277 multiple-target variables with high accuracy (Zhou et al., 2024; Fu et al., 2023;
278 Cummins et al., 2023; Cummins et al., 2024). Additionally, the technique enables the
279 seamless integration of physical constraints, improving the reasonableness of the results
280 (Zhou et al., 2024; Zhao et al., 2019; Shang et al., 2023).

281 In order to estimate the SHF and LHF with high accuracy in a physics-consistency
282 framework, the β (= SHF/LHF) physical constraint was incorporated into the NN model
283 using the custom multiple-objects (SHF, LHF and β) loss function as follows:

$$284 \quad LOSS = a \times LOSS_{SHF} + b \times LOSS_{LHF} + c \times LOSS_{\beta} \quad (12)$$

285 $LOSS_{SHF}$, $LOSS_{LHF}$ and $LOSS_{\beta}$ represent the Mean Squared Error (MSE) of SHF, LHF and
286 β , respectively. They were weighted using the factors of a (SHF), b (LHF) and c (β) to
287 balance the different magnitudes of loss during optimization. To prevent potential
288 gradient explosion during model training, predicted β [SHF'/LHF' , calculated using the
289 predicted SHF (SHF') and LHF (LHF')] values were clipped within the observed range

290 of β (from -5 to 5) during training:

$$291 \quad CLIP\left(\frac{SHF'}{LHF'}\right) = \begin{cases} \text{Min}\left(\frac{SHF'}{LHF'}, 5\right) & \frac{SHF'}{LHF'} > 0 \\ \text{Max}\left(\frac{SHF'}{LHF'}, -5\right) & \frac{SHF'}{LHF'} < 0 \end{cases} \quad (23)$$

$$292 \quad Loss_{\beta} = MSE\left(\frac{SHF'}{LHF'}, CLIP\left(\frac{SHF'}{LHF'}\right)\right) \quad (34)$$

293 Finally, after optimization, the final weights (a, b and c) for SHF, LHF, and β were
294 set to 5, 1, and 250, respectively. The model was constructed consisting of one input
295 layer, three hidden layers, two BatchNormalization layers, and one output layer using
296 the Python TensorFlow library. The numbers of neurons in the three hidden layers were
297 32, 64, and 16, respectively and the activation function of Leaky Rectified linear unit
298 (ReLU) was used throughout the model.

299 To illustrate the superiority of the BrTHF model in terms of accuracy and physical
300 consistency, another physics-free NN models, trained without integrating the β
301 constraint, were also constructed to predict SHF and LHF separately for further
302 comparison, where β was calculated to be SHF/LHF.

303 2.4 Evaluation strategy

304 A spatial 10-fold cross-validation was employed to assess the performances of the
305 BrTHF model for estimating air-sea SHF, LHF and β . Compared to the traditional 10-
306 fold cross-validation, which randomly split all samples into ten folds and thus may
307 result in overlapping spatial samples between training and validating datasets, the
308 spatial 10-fold cross-validation ~~were was~~ conducted in a relatively independent spatial
309 distribution and can provide a more robust and generalizable ~~generalized and~~
310 ~~convincing~~ evaluation.

311 Specifically, first, all buoy sites were randomly split into ten folds. Then, each fold
312 was in succession selected as the validation dataset and the remaining nine folds ~~rest of~~
313 ~~ten folds~~ was used as the training dataset.

314 The metrics used to evaluate the performance of the models include: (1) the mean
315 bias error (BIAS); (2) the root mean squared error (RMSE); (3) the correlation

316 coefficient (r):

$$317 \quad BIAS = \frac{1}{n} \sum_{i=1}^n (\hat{y}_i - y_i) \quad (45)$$

$$318 \quad RMSE = \sqrt{\frac{1}{n} \sum_{i=1}^n (\hat{y}_i - y_i)^2} \quad (56)$$

$$319 \quad r = \frac{\sum_{i=1}^n [(\hat{y}_i - \bar{\hat{y}})(y_i - \bar{y})]}{\sqrt{\sum_{i=1}^n (\hat{y}_i - \bar{\hat{y}})^2 \sum_{i=1}^n (y_i - \bar{y})^2}} \quad (67)$$

320 where n is the number of samples, \hat{y}_i and y_i are the estimated value and reference
321 truth, $\bar{\hat{y}}$ and \bar{y} are the mean of \hat{y}_i and y_i , respectively. These metrics—BIAS,
322 RMSE, and r —comprehensively evaluate model performance, representing systematic
323 deviation, dispersion between observations and estimates, and the strength and
324 direction of the linear relationship, respectively. Note that RMSE and r can be sensitive
325 to extreme values, particularly for the β , which is a ratio-based variable and may exhibit
326 unrealistically large magnitudes under near-zero flux conditions. To ensure a fair
327 evaluation, model performance is assessed both with all samples retained and with
328 extreme β values excluded in subsequent analyses. This dual evaluation allows us to
329 quantify overall model performance while explicitly accounting for the influence of
330 rare extreme cases.

331

332 **3. Results and discussion**

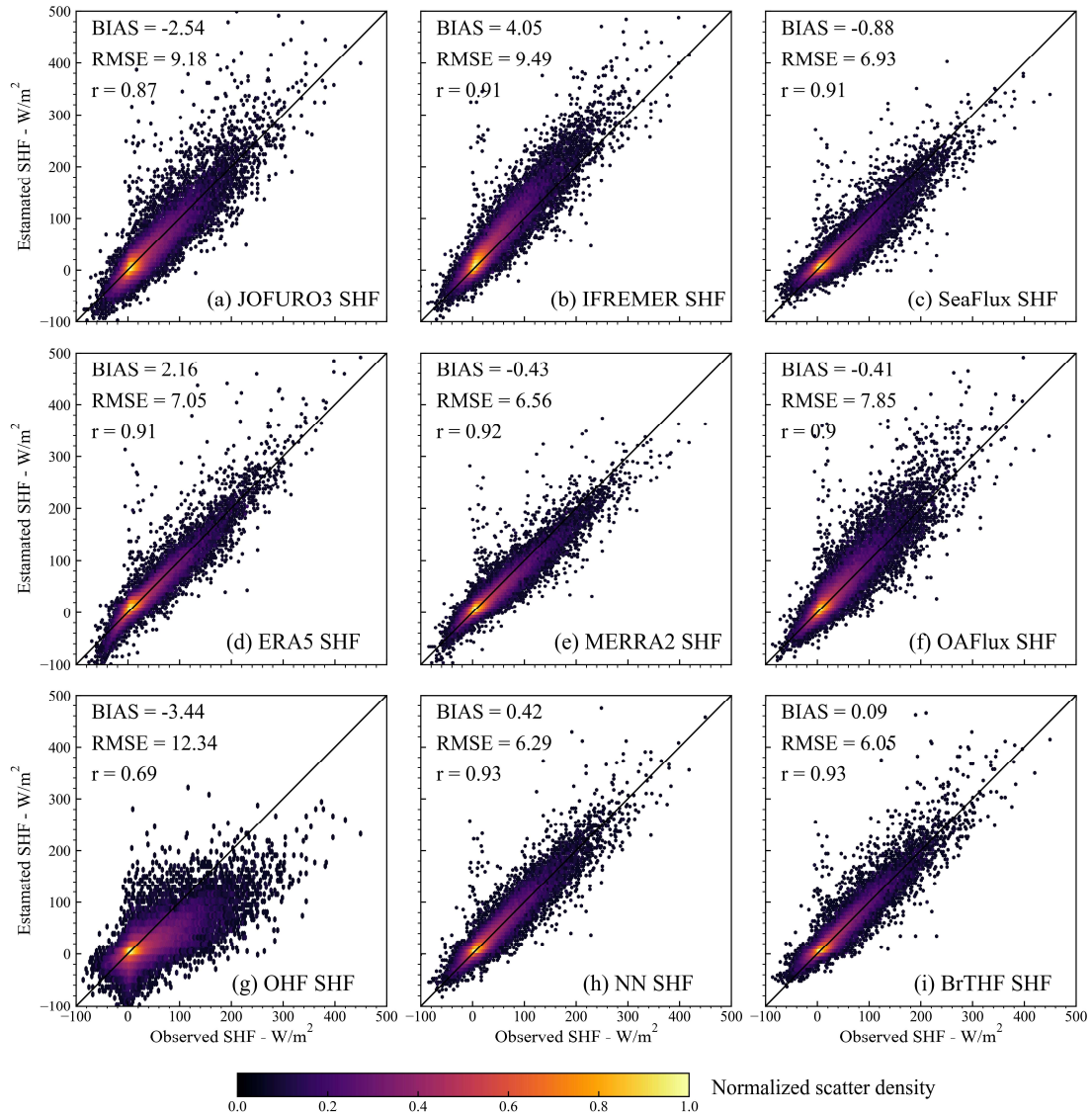
333 **3.1 Spatial ten-fold cross-validation of the models**

334 **3.1.1 Overall accuracy**

335 Figures 3, 4 and 5 present the normalized scatter density plots of the estimated
336 daily SHF, LHF and β from the BrTHF and physics-free NN models, as well as the
337 seven air-sea turbulent heat fluxes products against the observations obtained from 197
338 global distributed buoys by the spatial ten-fold cross-validation strategy.

339 Most models and products showed data distributions closely aligned with the
340 observed SHF, with the majority of samples clustered around the 1:1 line. The BrTHF
341 model slightly overestimated SHF with a BIAS of 0.09 W/m², whereas the physics-free

342 NN models, and ERA5 and IFREMER products showed more pronounced
343 overestimations (from 0.42 W/m² to 4.05 W/m²). In contrast, the remaining ~~rest~~-five
344 products exhibited notable underestimations (from -3.44 W/m² to -0.41 W/m²). As
345 illustrated in Figure 6, the variability of estimated SHF from the BrTHF and the
346 physics-free NN models and ERA5 product closely matched the observed SHF, all with
347 a Standard Deviation (STD) of approximately 16 W/m². Notably, the BrTHF model
348 achieved the lowest RMSE (6.05 W/m²), outperforming both the physics-free NN
349 models (6.29 W/m²) and the seven air-sea turbulent heat flux products (ranging up to
350 12.34 W/m² for OHF). Additionally, the BrTHF model combined with the physics-free
351 NN models yielded the highest values of r (0.93), surpassing all seven other products.
352 In summary, the BrTHF model showed ~~overall~~-the best overall performance in
353 estimating SHF among all the models and products.

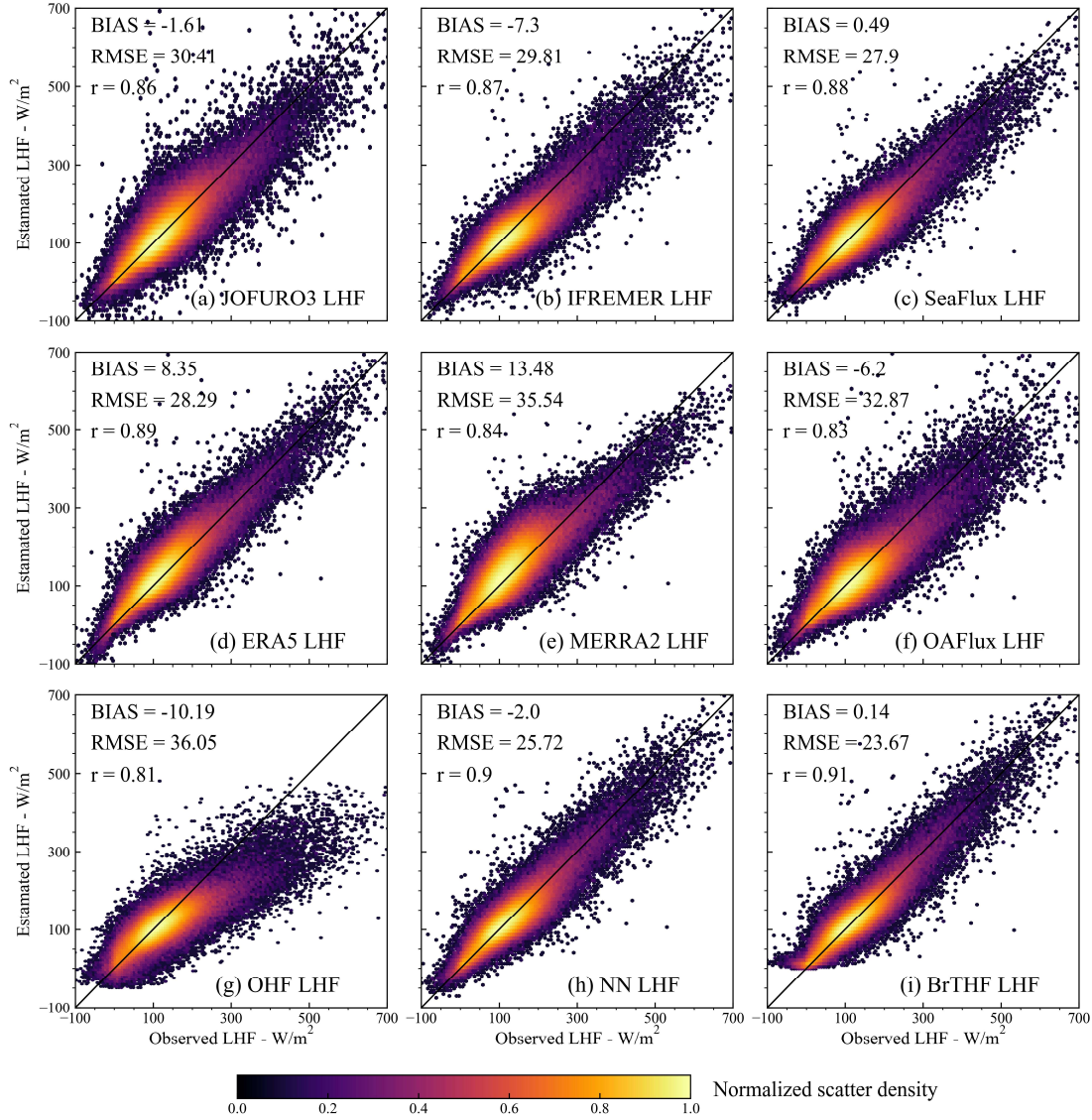


354

355 **Figure 3. Normalized scatter density plots of estimated SHF from the BrTHF model, the**
 356 **physics-free NN models and seven air-sea turbulent heat fluxes products against the observed**
 357 **SHF obtained from 197 global distributed buoys.**

358 For LHF, similar to the results for SHF, the BrTHF model ~~also~~ demonstrated the
 359 best agreement with observations, achieving the lowest RMSE (23.67 W/m²) and the
 360 highest value of r (0.91). Compared to the physics-free NN models and seven products,
 361 the BrTHF model reduced RMSE by 2.05 W/m² (physics-free NN models) to 12.38
 362 W/m² (OHF) and improved r by 0.01 (physics-free NN model) to 0.1 (OHF).
 363 Additionally, the BrTHF model showed a slight overestimation of LHF (BIAS = 0.14
 364 W/m²), lower than that of the SeaFlux, MERRA2, and ERA5 products. In contrast, the

365 remaining products (JOFURO3, IFREMER, OAFlux, and OHF), along with the
 366 physics-free NN models, underestimated LHF, with the BIAS values ranging from -
 367 10.19 W/m² (OHF) to -1.61 W/m² (JOFURO3).

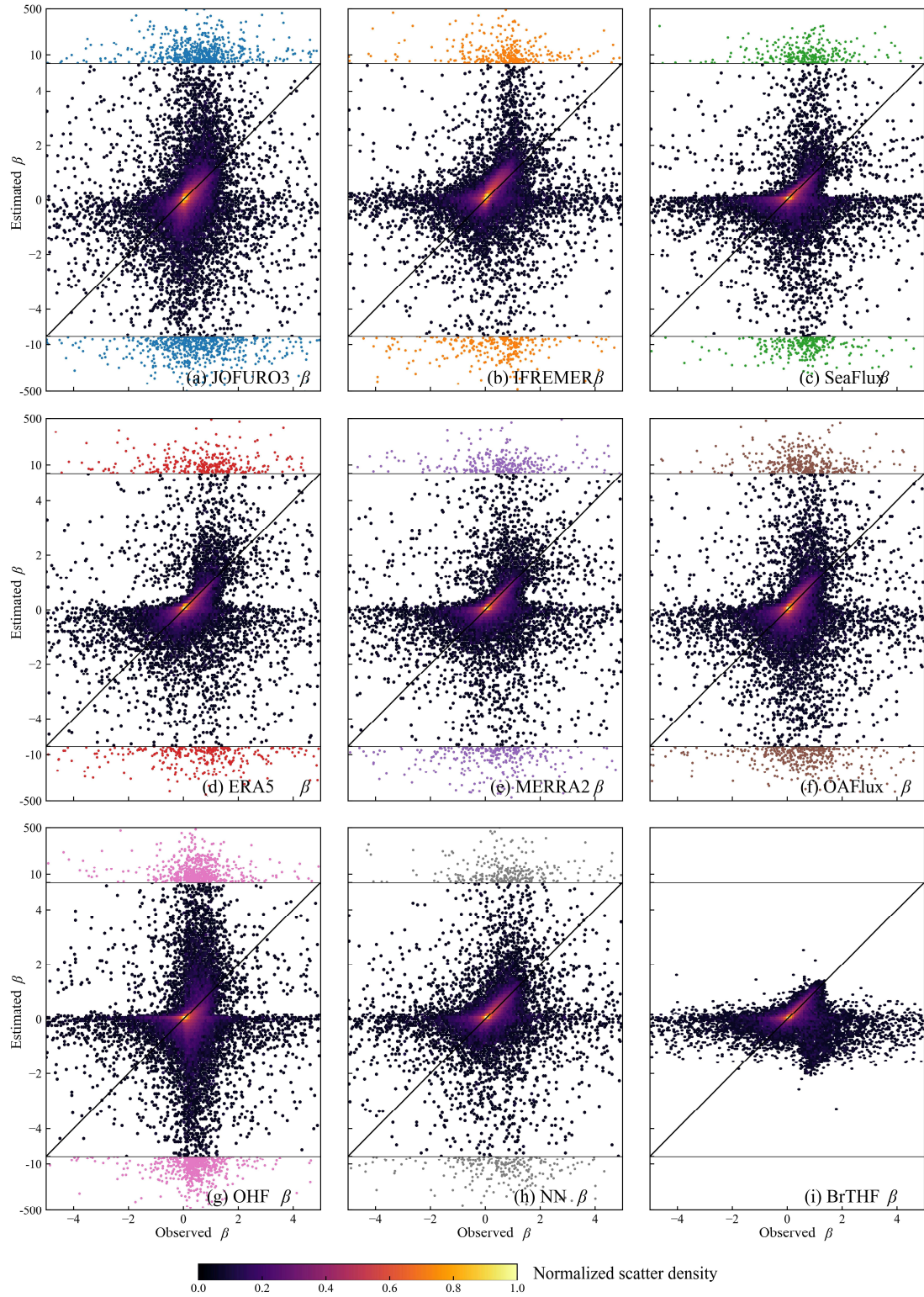


368

369 **Figure 4. Same as Figure 3 but for LHF.**

370 The BrTHF model exhibited a significantly different distribution of β compared to
 371 the physics-free NN models and the seven products, as shown in Figure 5. The β
 372 estimates from the BrTHF model consistently fell within the observed range of -5 to 5,
 373 while the physics-free NN model and the seven products occasionally produced
 374 estimates outside this range. Specifically, approximately 0.9% of β estimates from both
 375 the physics-free NN model and the seven products were out of range. The extreme

376 positive and negative β estimates were found in the OHF ($\beta = 14997$) and physics-free
377 NN models ($\beta = -25703$) products, respectively. The abnormal β estimates significantly
378 impacted the accuracy of the physics-free NN models and the seven products as Figure
379 6 indicated. When excluding the abnormal β samples from the physics-free NN models
380 and seven products, the RMSEs ranged from 0.17 (physics-free NN models and
381 SeaFlux) and 0.26 (OHF), with values of r ranging from 0.13 (OHF) to 0.46
382 (IFREMER), as shown in Figure 6 and Table S3. However, when all estimates were
383 considered, the performances of these model and products deteriorated sharply, with
384 RMSEs rising from 0.87 (SeaFlux) to 39.21 (physics-free NN models), and values of r
385 dropping from 0.06 (SeaFlux) to 0 (JOFURO3, MERRA2 and OHF). In contrast, the
386 BrTHF model maintained robust outperformance, with the lowest RMSEs of 0.22 and
387 0.15, and higher r values of 0.25 and 0.43, both before and after removing the abnormal
388 β samples from the physics-free NN models and the seven products. Notably, the BIAS
389 values remained stable (ranging from -0.04 to 0.04) for all models and products,
390 regardless of whether the abnormal samples were excluded.



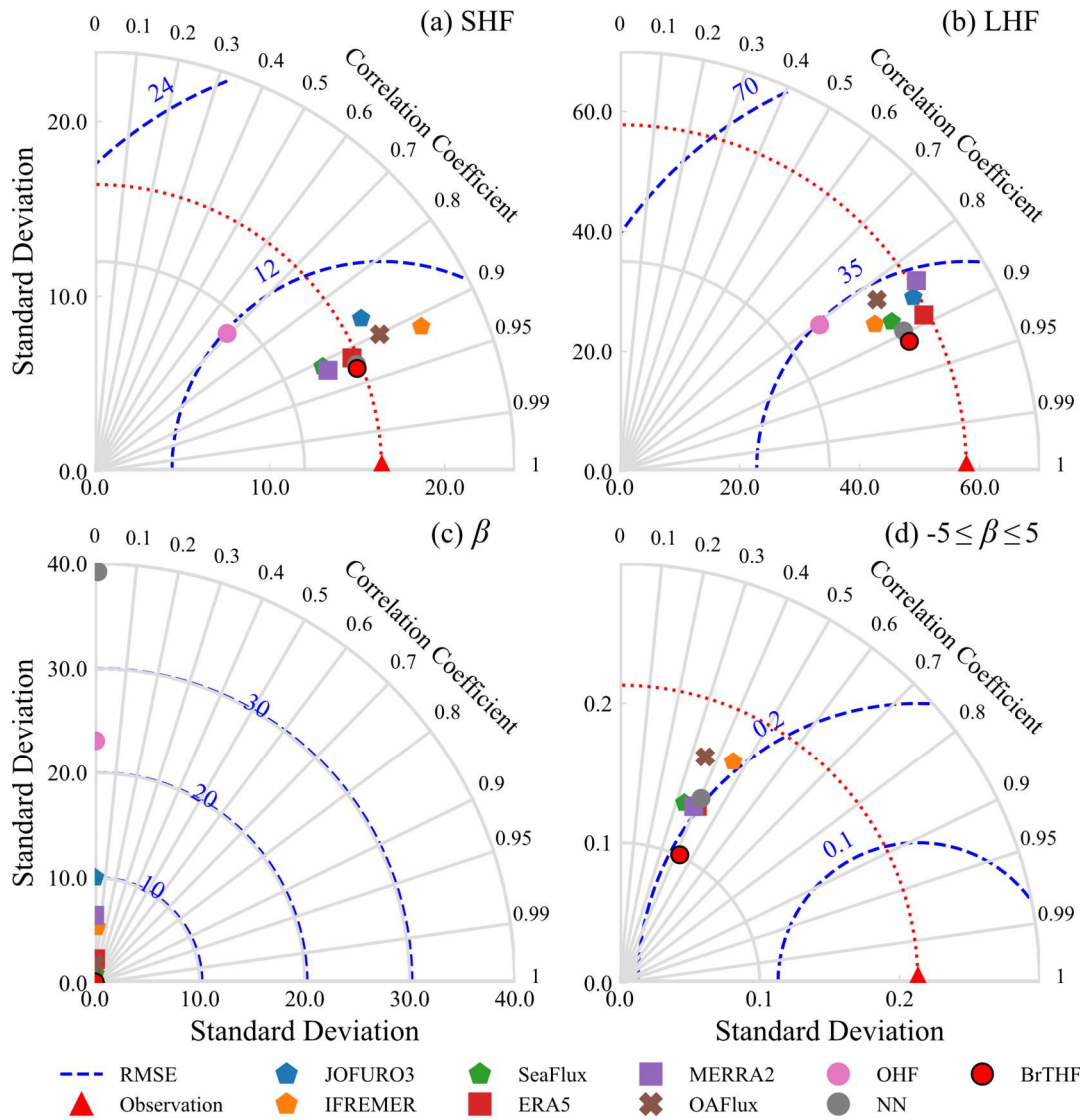
391

392 **Figure 5. Same as Figure 3 but for β . The samples out of the ranges of observed β ($-5 \leq \beta \leq 5$)**

393 **were colored in blue, orange, green, red, purple, brown, pink and gray for JOFURO3,**

394 **IFREMER, SeaFlux, ERA5, MERRA2, OAFflux, OHF products and the physics-free NN**

395 **models, respectively. The statistical metrics could be found in Table S3 and Figure 6.**



396

397 **Figure 6. Taylor diagrams of the validation of estimated daily SHF (a), LHF (b), β (c) (-**
 398 **$5 \leq \beta \leq 5$, d) from the BrTHF model, the physics-free NN models and the seven products against**
 399 **the in-situ observations.**

400

401 3.1.2 Accuracies across oceans

402 To better understand the accuracy of SHF, LHF and β estimates from the BrTHF
 403 and physics-free NN models, as well as the seven products in different oceans, we
 404 conducted an additional evaluation by categorizing the observations according to the
 405 belonging ocean basins, as shown in Figure 7. The major ocean boundaries, obtained
 406 from Marine Regions (<https://www.marineregions.org/>), were used to define the ocean

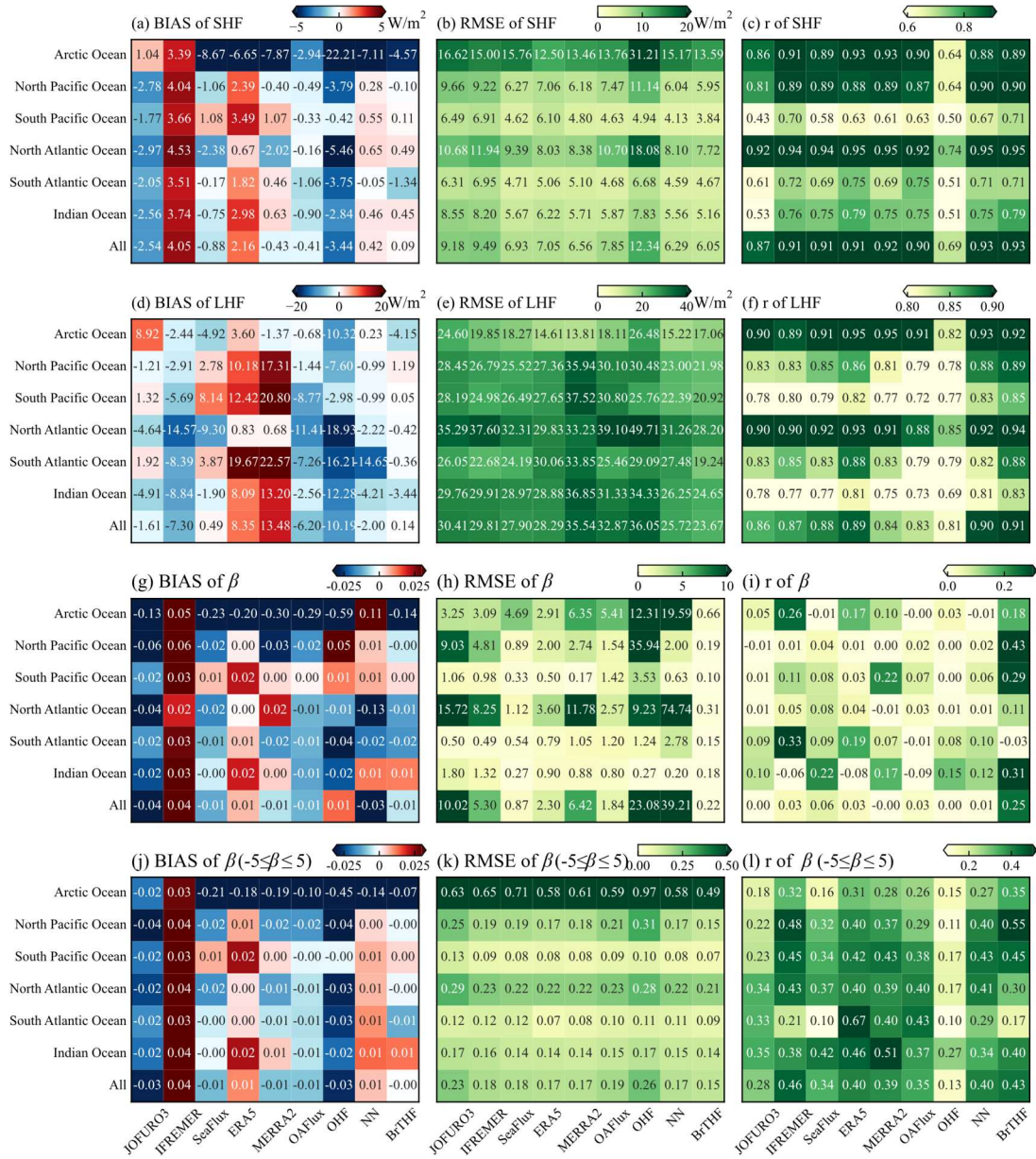
407 basins, which include the Arctic Ocean, South Pacific Ocean, North Pacific Ocean,
408 South Atlantic Ocean, North Atlantic Ocean, and Indian Ocean.

409 For SHF, the BrTHF model exhibited overestimations in the South Pacific Ocean,
410 North Atlantic Ocean, and Indian Ocean, while it underestimated SHF in the remaining
411 three ocean basins. The values of BIAS ranged from -4.57 W/m^2 in the Arctic Ocean to
412 0.49 W/m^2 in the North Atlantic Ocean. Furthermore, the BrTHF achieved the lowest
413 RMSEs in most ocean basins, ranging from 3.84 W/m^2 in the South Atlantic Ocean to
414 7.72 W/m^2 in the North Atlantic Ocean, except in the Arctic Ocean where the RMSE of
415 13.59 W/m^2 ~~was~~ ere higher than those of the ERA5 (12.5 W/m^2) and MERRA2 (13.46
416 W/m^2) products, as shown in Figure 7(b). Correlation analysis also demonstrated the
417 robust performance of the BrTHF model in estimating SHF, with values of r exceeding
418 0.89 in most ocean basins, except ~~for those~~ for those ocean basins in the Southern Hemisphere
419 (ranging from 0.71 to 0.79) where the values of r for all models and products were
420 reduced.

421 For LHF, the values of BIAS of the BrTHF model ranged from -4.15 W/m^2 in the
422 Arctic Ocean to 1.19 W/m^2 in the North Pacific Ocean. In comparison, the BrTHF
423 model showed more pronounced underestimations in the Arctic Ocean and Indian
424 Ocean. Additionally, the BrTHF model outperformed the physics-free NN models and
425 the seven products across most ocean basins, achieving the lowest RMSEs (ranging
426 from 17.06 W/m^2 in the Arctic Ocean to 28.20 W/m^2 in the North Atlantic Ocean) and
427 the highest values of r (ranging from 0.83 in the Indian Ocean to 0.94 in the North
428 Atlantic Ocean) except for the Arctic Ocean where the value of r was 0.01 less than the
429 physics-free NN models and the RMSE were 2.45 W/m^2 , 3.25 W/m^2 and 1.84 W/m^2
430 higher than the ERA5 and MERRA2 products and the physics-free NN models,
431 respectively. Combining the overall and regional evaluations, we find that, except for
432 the OHF product, the relative performance of SHF and LHF among the seven products
433 is generally consistent with Tang et al. (2024). The OHF product shows notable
434 degradation, particularly in high-latitude oceans, which may be due to limitations in the

435 training datasets (sparse and unevenly distributed in-situ observations) and model
436 training strategy (randomly splitting all observations into training, validation, and test
437 sets without accounting for spatial dependencies), leading to reduced transferability.

438 The BrTHF model consistently performed better in estimating β across most ocean
439 basins, both before and after removing the abnormal β samples that deviated from the
440 observed range ($-5 \leq \beta \leq 5$). In contrast, the physics-free NN models and the seven
441 products did not perform as well. Specifically, the BrTHF model exhibited the lowest
442 RMSEs in almost all ocean basins except in the South Atlantic Ocean after removing β
443 outliers. Moreover, in terms of correlation analysis, the BrTHF model achieved higher
444 values of r in most ocean basins before and after the removal of abnormal β samples,
445 among all models and products.
446



447

448 **Figure 7. Heatmaps of BIAS, RMSE and r metrics for the validation of estimated daily SHF**

449 **(a - c), LHF (b - e), β (f - i) and $\beta (-5 \leq \beta \leq 5)$ (j - l) from the BrTHF model, the physics-free NN**

450 **models and the seven products against the in-situ observations across different ocean basins.**

451 **It should be noted that the statistical metrics for each ocean basin were calculated using**

452 **observations from the available buoys within the corresponding basin.**

453

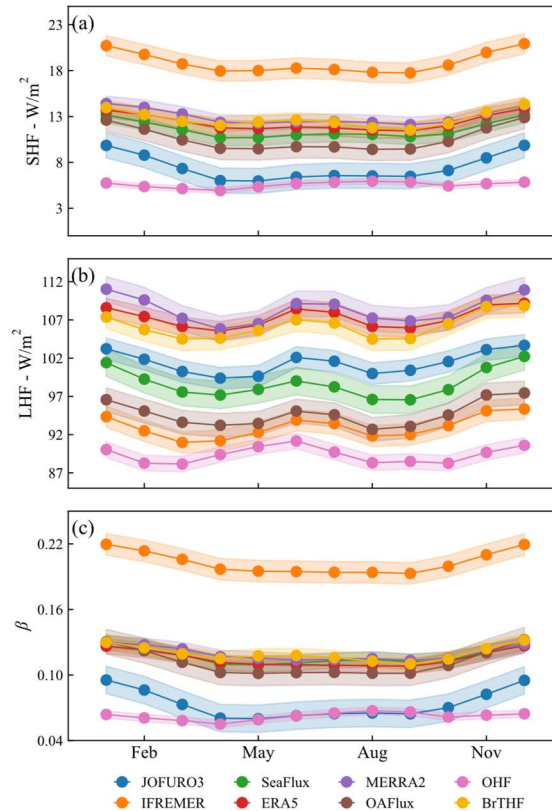
454 3.2 Temporal variations in SHF, LHF and β

455 After spatial ten-fold cross-validation, we produced the daily 0.25° global air-sea

456 turbulent heat fluxes products from 1993 to 2017 using a combination of the BrTHF

457 model and learning datasets, and further made a comparison of the temporal variation
458 (in this section), spatial distribution (in Section 3.3) and annual trend (in Section 3.4)
459 of SHF, LHF and β estimates from the BrTHF product and those with the seven state-
460 of-the-art global products. The selected period (from 1993 to 2017) was determined by
461 the overlapping availability of input learning datasets.

462 Figure 8 illustrates the monthly area-weighted global means of SHF, LHF and β
463 from 1993 to 2017 for the BrTHF product and seven state-of-the-art products. The
464 BrTHF product exhibited similar bimodal patterns for SHF, LHF and β as the seven
465 products, with peaks in December-January and May-June-July-August. In addition, the
466 peak in May-June-July-August was less pronounced for SHF and β compared to that
467 for LHF. The monthly area-weighted global means of SHF and β from the BrTHF
468 product were higher than those of most products, except for the MERRA2 product in
469 January, February, March, April, July, August and September, and the IFREMER
470 product in all months. For LHF, the BrTHF showed lower values than the ERA5 and
471 MERRA2 products across all months. Notably, the patterns of SHF and β from the OHF
472 product, with the highest peak occurring in August and smoother intra-annual cycles,
473 differed from those of the corresponding BrTHF product and the other six products
474 developed using the bulk aerodynamic methods.

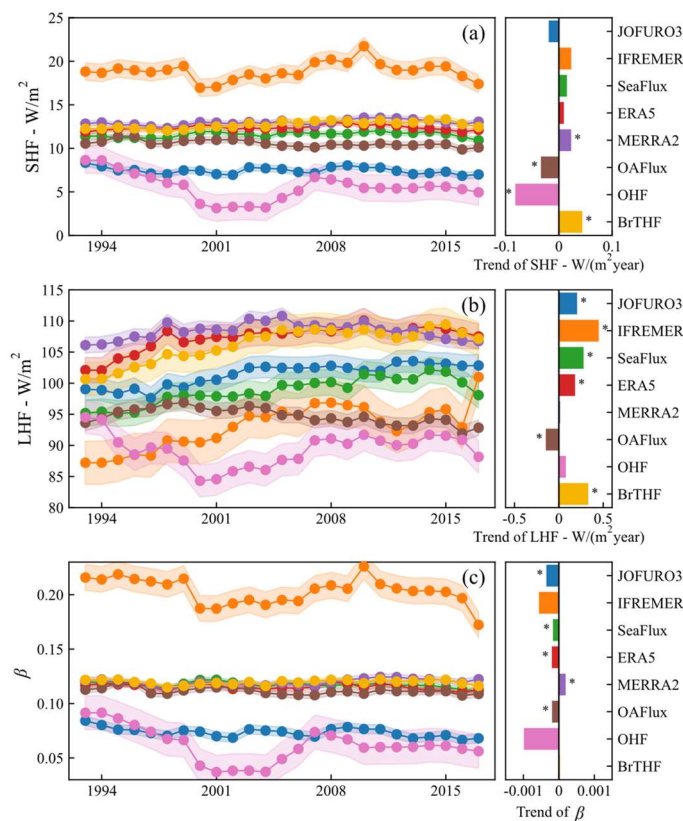


475

476 **Figure 8. Intra-annual cycles of area-weighted global monthly mean of SHF (a), LHF (b) and**
 477 **β (c) from the eight products from 1993 to 2017. The shaded areas indicate ± 1 standard**
 478 **deviation around the mean.**

479 Figure 9 presents the temporal evolution of the area-weighted annual global mean
 480 of SHF, LHF and β from 1993 to 2017 for the eight products ~~for the over~~ ice-free oceans.
 481 The global mean annual SHF of the BrTHF product was 12.7 W/m^2 , which was close
 482 to those of SeaFlux (11.6 W/m^2), OAFflux (10.6 W/m^2), MERRA2 (13 W/m^2) and
 483 ERA5 (12.4 W/m^2), whereas ~~it~~ significantly lower than that of IFREMER (18.8 W/m^2)
 484 and higher than those of JOFURO3 (7.5 W/m^2) and OHF (5.6 W/m^2). Meanwhile, the
 485 BrTHF product exhibited ~~the largest significant increases~~ ~~significant largest growth~~ of
 486 SHF with the trend of $0.04 \text{ W}/(\text{m}^2 \cdot \text{year})$ among all eight products, and showed similar
 487 temporal evolution as SeaFlux, MERRA2, ERA5 and OAFflux during the period from
 488 1993 to 2017. As for LHF, the BrTHF exhibited a ~~relatively high~~ ~~larger~~ global mean
 489 annual value of 106.2 W/m^2 , which was close to those of the ERA5 (107.3 W/m^2) and
 490 MERRA2 (108.3 W/m^2), and it was significantly higher than ~~the~~ rest of the products.

491 Moreover, the growth of the BrTHF LHF was significant with a trend of 0.33
 492 $W/(m^2 \cdot year)$, which was lower than the IFREMER but higher than the OAFflux,
 493 MERRA2, OHF, ERA5, JOFURO3 and SeaFlux, ranging from $-0.14 W/(m^2 \cdot year)$ to
 494 $0.4 W/(m^2 \cdot year)$. Note that only the OAFflux product showed a negative trend of LHF
 495 from 1993 to 2017. For β , the BrTHF showed a similar temporal pattern to that of SHF,
 496 and most products concentrated within the narrow range of 0.11 to 0.12 for the annual
 497 values. The magnitude of annual β of the BrTHF was about 0.11, which was close to
 498 the OAFflux, SeaFlux, MERRA2 and ERA5, but significantly lower than the IFREMER
 499 and higher than the JOFURO3 and OHF. Moreover, in contrast to the significant
 500 increasing trends of LHF and SHF, negative ~~of~~-trends of β were shown for most
 501 products. However, the BrTHF product exhibited a weak positive trend, which may be
 502 attributed to the relatively smaller differences between the SHF and LHF trends in
 503 BrTHF compared to those in other products.



504

505 **Figure 9. Inter-annual evolution of area-weighted global mean SHF (a - b), LHF (c - d) and β**

506 **(e - f) from 1993 to 2017. The trends were calculated based on the Sen's slope method. The ***

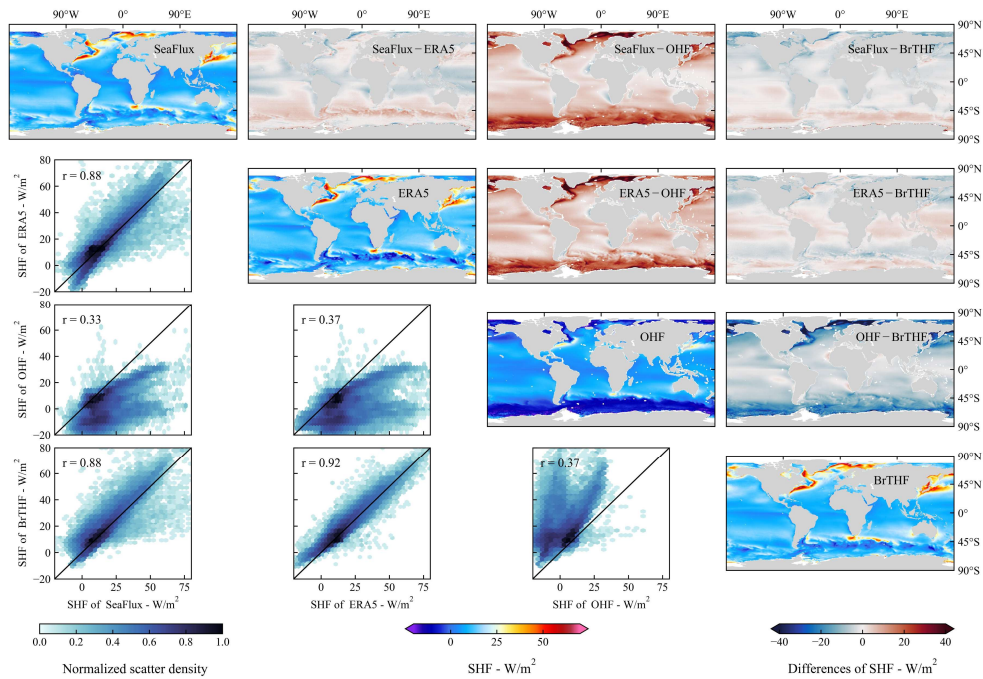
507 in the sub-figures (b, d and f) represent the trend passed the Mann-Kendall significant test (p
508 < 0.05). The shaded areas indicate ± 1 standard deviation around the mean.

509

510 3.3 Inter-comparison of the spatial pattern

511 We selected three representative products including the (reanalysis-based) ERA5,
512 (remote sensing-based) SeaFlux, and (the only publicly available machine learning-
513 based) OHF products to evaluate the BrTHF product's ability in simulating global air-
514 sea turbulent heat fluxes (SHF, LHF, and β) from 1993 to 2017. These products were
515 chosen because they demonstrated relatively high accuracy within their respective
516 categories (as shown in Section 3.1) and shared the same 0.25° spatial resolution with
517 the BrTHF product.

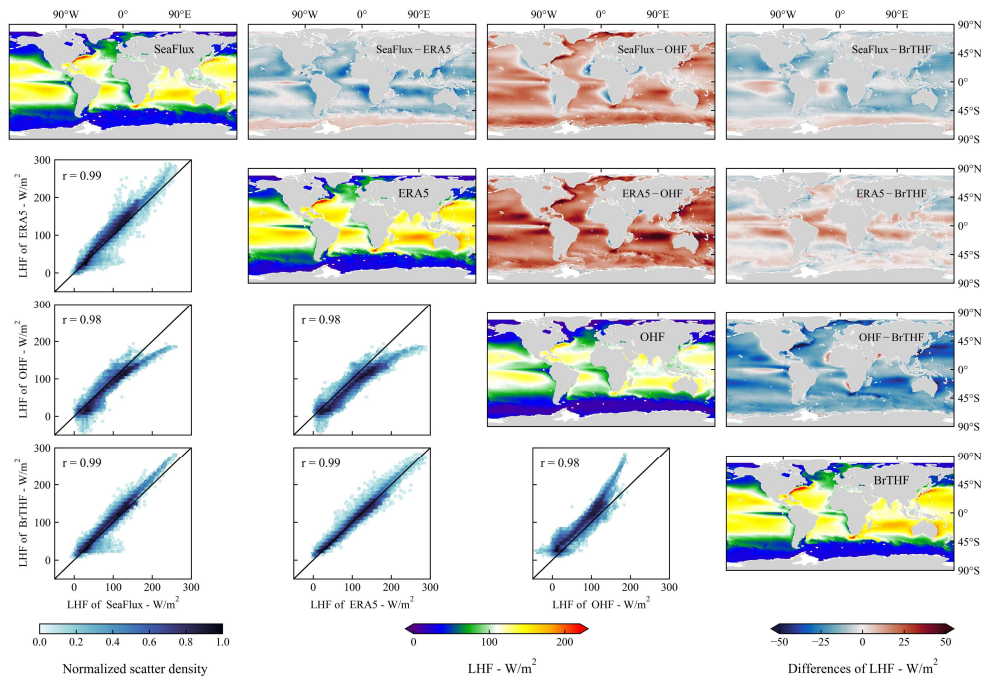
518 Figure 10 presents the spatial distribution of multi-year mean of SHF from the
519 SeaFlux, ERA5, BrTHF, and OHF products, along with their cross-comparisons.
520 Overall, the BrTHF product exhibited strong consistency with ERA5 and SeaFlux
521 products, with values of r exceeding 0.88, which was significantly higher than the
522 consistency between SeaFlux and OHF ($r = 0.33$) and between ERA5 and OHF ($r =$
523 0.37). Spatially, the BrTHF, SeaFlux and ERA5 products all showed higher SHF (over
524 50 W/m^2) in the Western Boundary Currents (WBCs, e.g. Kuroshio, Gulf Stream, Brazil
525 Current and Agulhas Current) regions, whereas the OHF product yielded much lower
526 SHF ($\sim 25 \text{ W/m}^2$). Additionally, the former three products captured pronounced SHF
527 gradients in the Southern Ocean, features that were absent in the OHF product. SHF
528 differences between BrTHF and SeaFlux/ERA5 remained within $\pm 10 \text{ W/m}^2$ in most
529 oceans. The BrTHF product exhibited slightly higher SHF values than SeaFlux in the
530 Northern Hemisphere, whereas in the Southern Hemisphere—particularly over the
531 Southern Ocean—the BrTHF showed relatively lower SHF. Compared to the ERA5
532 product, the BrTHF product yielded lower SHF in the equatorial zone, subtropical high-
533 pressure regions and the Southern Ocean, but higher SHF in other areas, particularly in
534 the North Pacific and the southern Indian Ocean.



535

536 **Figure 10. Inter-comparison of the spatial distributions of multi-year means of SHF among**
 537 **the SeaFlux, ERA5, OHF and BrTHF products from 1993 to 2017.**

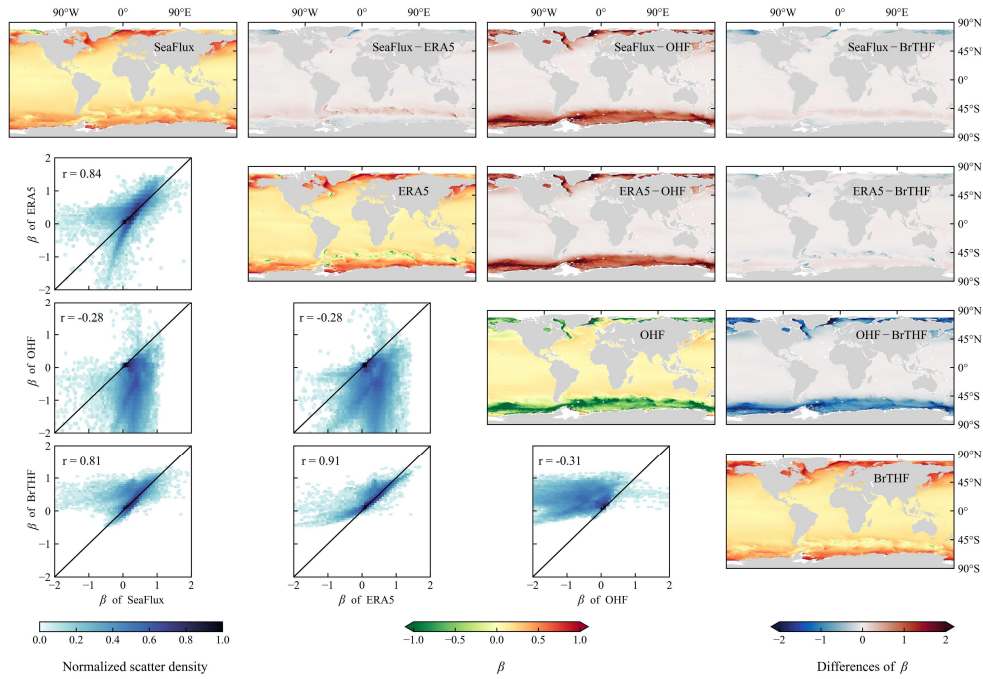
538 For LHF, the BrTHF and the ~~selected~~-three reference products exhibited more
 539 similar ~~close~~-spatial distribution patterns, with the values of r exceeding 0.98, compared
 540 to the results for the SHF, as shown in Figure 11. The higher LHF (over 150 W/m^2)
 541 primarily occurred around the regions of WBCs and the sub-tropic highs, while lower
 542 LHF (below 50 W/m^2) appeared in the Eastern Equatorial Pacific and Atlantic Warm
 543 Tongue and the oceans with latitudes higher than 45° . The spatial distribution of LHF
 544 in the BrTHF product generally agreed better with that of the ERA5 product, though
 545 the BrTHF showed significantly lower LHF in sub-tropic highs. Additionally, the
 546 BrTHF exhibited relatively lower LHF than the ERA5 over the Southern Ocean and the
 547 central North Atlantic. Compared to the SeaFlux, the BrTHF yielded slightly higher
 548 LHF in most oceans except the Southern Ocean and equatorial zones.



549

550 **Figure 11. Same as Figure 10 but for LHF.**

551 For β , the BrTHF product demonstrated strong spatial correlation with the ERA5
 552 and SeaFlux in multi-year mean distributions, with values of r exceeding 0.81. In
 553 contrast, the OHF showed a markedly ~~a~~ different spatial pattern of β , exhibiting
 554 negative correlations when compared to the ~~rest of other~~ three products. Spatially, the
 555 BrTHF product's β distribution aligned more closely with the SeaFlux, both displaying
 556 higher β (up to 1) in high-latitude oceans particularly in the Northern Hemisphere and
 557 the similar wavelike textures of β over the Southern Ocean's Antarctic Circumpolar
 558 Current zone. The differences between the BrTHF and OHF products were more
 559 evident. Specifically, the BrTHF product showed overall overestimation of β in the
 560 oceans where latitudes were larger than 45° compared to the OHF product.



561

562 **Figure 12. Same as Figure 10 but for β .**

563

564 3.4 Spatial pattern of trends in SHF, LHF and β from the BrTHF product

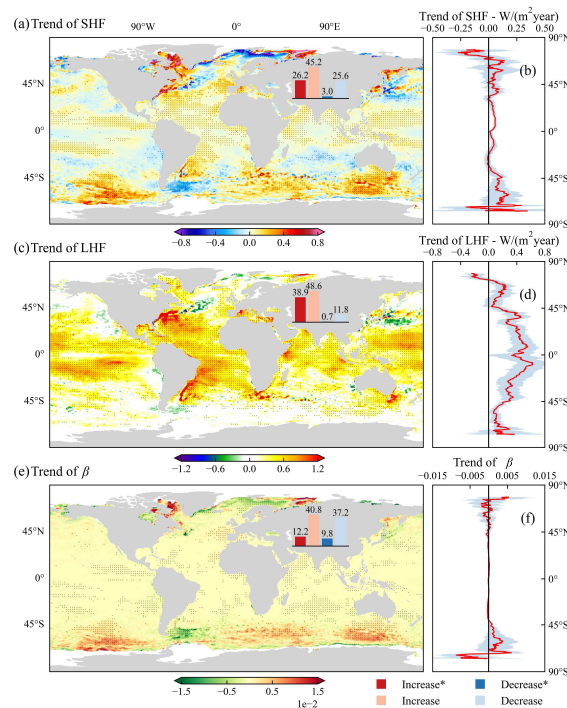
565 Figure 13 illustrates the spatial distribution of inter-annual trends of SHF, LHF and
 566 β in the BrTHF product from 1993 to 2017. The SHF showed increasing trends across
 567 71.4% of the oceans, with statistically significant increases in 26.2% of regions. In
 568 contrast, decreasing trends were observed in 28.6% of the oceans, with only 3%
 569 showing significant reductions. Overall, the trends of zonal annual averages of SHF
 570 remained stable between ~~the~~ 60°N to 45°S , with significant increases occurring
 571 southward and decreases northward. Specifically, moderate increases ($\sim 0.2 \text{ W}/(\text{m}^2$
 572 year)) dominated between 45°N and 45°S , while more pronounced increases (> 0.8
 573 $\text{W}/(\text{m}^2 \text{ year})$) were observed in mid- and high-latitude oceans, including the Kara Sea,
 574 Gulf Stream, Baffin Bay, Brazil Current, Sea of Okhotsk, and Sea of Japan. Notable
 575 decreases ($< -0.8 \text{ W}/(\text{m}^2 \text{ year})$) were concentrated in the Barents Sea and the central
 576 North Atlantic.

577 The LHF exhibited markedly different characteristics of the spatial distribution,
 578 with 87.5% of oceans showing increasing trends (38.9% were significant), versus 12.5%
 579 decreasing (0.7% were significant). In contrast to those of the SHF, the trends of zonal

580 annual averages for LHF weakened poleward from the oceans of Equator. The
 581 substantial increases ($>0.6 \text{ W}/(\text{m}^2 \text{ year})$) occurred in the oceans between
 582 45°N to 45°S , particularly in the Gulf Stream, Brazil Current, and Agulhas Current
 583 systems, while notable decreases (lower than $-0.3 \text{ W}/(\text{m}^2 \text{ year})$) were
 584 observed in the central North Atlantic and Kuroshio extension regions.

585 For β , approximately 53% of the oceans showed increasing trends, with 12.2% of
 586 these being statistically significant. Conversely, about 47% of the oceans showed
 587 decreasing trends, with 9.8% being significant. Most oceans between 45°N to 45°S
 588 exhibited near-zero trends, while significant trends were concentrated in the high-
 589 latitude oceans. Notable increases were found in Baffin Bay, Kara Sea, and the Southern
 590 Ocean, while decreases were observed in the Barents Sea and the Southern Ocean near
 591 South America.

592



593

594 **Figure 13. Spatial maps of inter-annual trends for SHF (a), LHF (c), and β (e) from the BrTHF**
 595 **product for the period 1993 to 2017. The trends were calculated using the Sen's slope method.**

596 **Dotted areas indicate oceans where the p-value of the Mann-Kendall significance test is less**

597 **than 0.05. Panels (b), (d) and (f) represent the inter-annual trends of zonal annual averages**

598 for SHF, LHF and β , respectively.

599 3.5 Discussion

600 Advancing our understanding of the air-sea interaction and achieving the global
601 closure of the ocean surface energy budget require accurate global-scale simulations of
602 air-sea turbulent heat fluxes (Yu, 2019). Existing global air-sea turbulent heat fluxes
603 products, primarily generated using the semi-empirical bulk aerodynamic methods and
604 data-driven machine learning approach, are often weak in accuracy and physical
605 rationality, arising from uncertainties in environmental forcings and inappropriate
606 parameterizations (Brodeau et al., 2017; Jiang et al., 2024a; Wang et al., 2024). To
607 improve the simulation of the global air-sea turbulent heat fluxes, this study presents
608 the BrTHF product, generated using a Bowen ratio-constrained NN technique with a
609 custom multiple-objective loss function, as well as observations from 197 globally
610 distributed buoys along with multi-source remote sensing and reanalysis inputs.

611 3.5.1 Advantages

612 ~~The primary advantage of the BrTHF product is the absence of outliers in the~~
613 ~~estimation of β . Unlike the approach of our previous study (Wang et al., 2024), which~~
614 ~~simultaneously predicted SHF, LHF and β in the constructed RF model, this study~~
615 ~~employed an NN model constrained by the Bowen ratio to jointly estimate SHF and~~
616 ~~LHF. The new approach avoided the issue of selection of β derived from either the~~
617 ~~calculated β [β_{cal} equals predicted SHF (SHF_{pre}) divided by predicted LHF (LHF_{pre})] or~~
618 ~~the predicted β (β_{pre}), as reported by Wang et al. (2024). Furthermore, the custom loss~~
619 ~~function in our new approach provides a flexible approach to adjust the weights of SHF,~~
620 ~~LHF, and β , allowing the model to balance attention among these variables. As a result,~~
621 ~~the accuracy of SHF, LHF, and β from our newly developed BrTHF model~~
622 ~~outperformed that of the mainstream air-sea turbulent heat fluxes products and the~~
623 ~~physics-free NN models on both global and regional scales. In contrast, the accuracy of~~
624 ~~SHF and LHF in the model constructed by Wang et al. (2024) was somewhat marginally~~
625 ~~lower than that of the physics-free RF model.~~

626 The primary advantage of the BrTHF model lies in its accurate estimation of β ,
627 which shows the most pronounced improvement among all flux components. As a key
628 indicator of surface energy partitioning, β is widely used within the surface energy
629 balance framework to ensure physically consistent and reliable estimates of SHF and
630 LHF (Yang et al., 2025). In addition, β serves as an effective diagnostic variable in the
631 studies of large-scale climate variability (e.g., ENSO) (Jo, 2002) and in investigations
632 of how surface energy constraints regulate the hydrological cycle (e.g., precipitation)
633 (Wang et al., 2021). With its enhanced representation of β , the BrTHF product is
634 expected to provide more reliable support for such applications.

635 To achieve these improvements in β and flux, the BrTHF model was designed
636 differently from our previous study (Wang et al., 2024), which simultaneously predicted
637 SHF, LHF and β in the constructed RF model. Specifically, this study employed an NN
638 model constrained by the Bowen ratio to jointly estimate SHF and LHF. The new
639 approach avoided the issue of selection of β derived from either the calculated β [β_{cal}
640 equals predicted SHF (SHF_{pre}) divided by predicted LHF (LHF_{pre})] or the predicted β
641 (β_{pre}), as reported by Wang et al. (2024). Furthermore, the custom loss function in our
642 new approach provides a flexible approach to adjust the weights of SHF, LHF, and β ,
643 allowing the model to balance attention among these variables. As a result, the accuracy
644 of SHF, LHF, and β from our newly developed BrTHF model outperformed that of the
645 mainstream air-sea turbulent heat flux products and the physics-free NN models on both
646 global and regional scales. In contrast, the accuracy of SHF and LHF in the model
647 constructed by Wang et al. (2024) was somewhat marginally lower than that of the
648 physics-free RF model.

649 3.5.2 Generalizability

650 ~~The machine learning-based OHF product demonstrated significantly poorer~~
651 ~~performance in estimating SHF and LHF, with higher RMSEs and lower values of r , as~~
652 ~~shown in Figure 6, compared to the remote sensing, reanalysis, and hybrid-based~~
653 ~~products developed using the bulk aerodynamic methods. This finding contrasted with~~

654 the results of Tang et al. (2024), who reported the superior performance of the OHF
655 product. The discrepancy could primarily be attributed to the different spatial
656 representativeness of the observation datasets used by Tang et al. (2024), which were
657 primarily collected from the buoys between 30°N and 30°S. Moreover, as shown in
658 Figure 7, the accuracy of the OHF product degraded notably in high-latitude ocean
659 basins, particularly in the North Atlantic Ocean. This accuracy degradation may be due
660 to the limitation of the observation datasets used to train the model of the OHF product,
661 where different sources of datasets were integrated, i.e. the SeaFlux in-situ dataset
662 (before 2007) and the ICOADS in-situ dataset (after 2007). Specially, the ICOADS in-
663 situ datasets, commonly used for developing products at monthly or lower frequency
664 scales (Berry and Kent, 2011; Gulev et al., 2013), suffered from sparse distribution and
665 insufficient volume for developing the original 3-hour OHF product. Besides, the model
666 of the OHF product was trained by randomly splitting all observations into training,
667 validation, and test sets, which likely resulted in data dependencies across these sets,
668 weakening the model's transferability. These problems together contributed to the
669 poorer performance of the OHF product, including worse accuracy, overall negative
670 spatial trends in high-latitude oceans such as the Southern Ocean, as Tang et al. (2024)
671 reported, and an overall underestimation of the multi-year mean, especially in the
672 Western Boundary Currents (WBCs) where the air-sea exchange is intense. In addition,
673 the OHF product did not reproduce similar large-scale spatial patterns of air-sea
674 turbulent heat fluxes observed in BrTHF, ERA5, and SeaFlux, which are primarily
675 shaped by atmospheric circulation and sea surface properties (e.g., sea surface
676 temperature and salinity).

677 Based on Figure 2 and Table S8, we observe that the spatial coverage of
678 observations varies across different ocean regions: the Northern Hemisphere generally
679 has higher coverage than the Southern Hemisphere, with the Northern Pacific Ocean
680 exhibiting the highest coverage, while the Arctic Ocean shows the lowest. Comparing
681 spatial coverage with accuracy metrics reveals a more complex relationship between

682 model performance and data coverage. Specifically, the values of r tend to be lower in
683 regions with lower coverage — a pattern consistent across SHF, LHF, and β . However,
684 RMSE does not follow this trend. For SHF and β , RMSEs in the Northern Hemisphere
685 are generally higher than those in the Southern Hemisphere. Similarly, for LHF, RMSEs
686 are higher in the Northern Hemisphere except in the Indian Ocean, where the pattern
687 differs.

688 We applied a spatial 10-fold cross-validation, which provides a more generalized
689 assessment than traditional random cross-validation, to evaluate the BrTHF model.
690 However, it is important to acknowledge that the spatial distribution of the training
691 dataset is inherently imbalanced, with a heavy concentration of observations in the
692 Tropics and the Northern Hemisphere. In contrast, the Southern Hemisphere—
693 particularly the Southern Ocean—suffers from sparse or even missing observational
694 coverage. Given that the environmental conditions in these underrepresented or data-
695 sparse regions may differ significantly from those captured in the training dataset, the
696 selected input variables for the observations may lead to large uncertainty in the model's
697 performance in these areas. To further assess the model's ability to extrapolate to such
698 regions, we conducted an additional targeted cross-validation. Specifically, we
699 excluded stations from the Southern Ocean [i.e., Southern Ocean Flux Station (SOFS)
700 and Global Southern Ocean Station (GSOS)] from the training dataset and used them
701 solely for validation. Results presented in Tables S4 and S5 show that the BrTHF model
702 achieved the best performance in terms of LHF and β at the SOFS with lower RMSE
703 of 15.6 W/m^2 and 0.73 and higher values of r of 0.96 and 0.34, respectively, while its
704 SHF was slightly outperformed by ERA5 and the physics-free NN model. At the GSOS,
705 BrTHF yielded more accurate estimates for SHF and β with RMSEs of 6.38 W/m^2 and
706 0.74 and values of r of 0.95 and 0.16, respectively, compared to other products, while
707 its LHF was marginally less accurate than that of SeaFlux and the physics-free NN
708 model. Moreover, under both spatially-informed cross-validation and targeted cross-
709 validation, the model demonstrates comparable accuracy at the two sites, as shown in

710 Figures S4–S7. These findings suggest that BrTHF retains competitive accuracy of SHF,
711 LHF and β even in regions entirely excluded from training, reflecting promising
712 generalization. While these results are encouraging, it is important to note that the
713 validation remains limited to a small number of sites with available observations.
714 Therefore, the reported r values and RMSE reflect model performance in these specific
715 locations and do not necessarily guarantee similar accuracy in broader, unobserved
716 ocean regions. Consequently, the BrTHF product should be viewed as being primarily
717 optimized within the geographical coverage of existing buoy networks. In remote
718 regions far from the observation-rich regions, such as the high-latitude Southern Ocean,
719 the lack of direct ground-truth constraints may result in certain uncertainties. Users
720 should therefore exercise caution when interpreting the global-scale performance,
721 particularly in data-sparse basins where spatial sampling limitations are most
722 pronounced.

723 The generalization capability of the model can also affect the accuracy of
724 simulated long-term trends. In Figure 13, we present the spatial distributions of long-
725 term trends for SHF, LHF, and β simulated by the BrTHF product. Considering the
726 scarcity of training data in high-latitude oceans, the simulated long-term trends in these
727 regions may be associated with larger uncertainties. However, due to the lack of long-
728 term observations in high-latitude oceans, we cannot validate the simulated trends using
729 observational records as has been done in previous studies for mid- and low-latitude
730 regions (Weller et al., 2022; Tang et al., 2024). To address this, we examined the spatial
731 distribution of long-term trends from the other seven widely used products. Specifically,
732 in these high-latitude regions, the trends simulated by the BrTHF are largely consistent
733 with those of most other products—for example, SHF exhibits a pronounced increase
734 in the Kara Sea, Gulf Stream, Baffin Bay, Brazil Current, Sea of Okhotsk, and Sea of
735 Japan, with differences mainly in magnitude.

736 3.5.3 Sensitivity and uncertainty

737 Given the key role of the β constraint in the BrTHF model, it is also important to

738 assess the sensitivity of the estimated SHF and LHF to the imposed β range. A series of
739 sensitivity experiments with progressively relaxed β constraints indicate that the BrTHF
740 model exhibits weak sensitivity to the specific choice of the β range (see Table S9). The
741 resulting variations in RMSE are small relative to their mean values, while values of r
742 and BIAS remain largely unchanged across different β configurations. These results
743 suggest that the improved performance of BrTHF is not driven by a particular
744 predefined range of β , but instead reflects the robustness of the Bowen ratio–
745 constrained machine learning framework.

746 Beyond the sensitivity to the imposed β range, we further examined the robustness
747 of the BrTHF model to uncertainties in its environmental inputs, using one-at-a-time
748 perturbation experiments (Table S10). The results indicate that the model is generally
749 insensitive to perturbations (from ± 5 to $\pm 20\%$) in most auxiliary inputs, with changes
750 in SHF and LHF RMSE typically remaining within 1%. Noticeable sensitivities are
751 mainly associated with WS , $diff_O$, and $diff_T$, which are physically expected given their
752 direct roles in controlling air–sea turbulent heat exchanges. Even under extreme
753 perturbations, the resulting variations in SHF and LHF remain within physically
754 reasonable ranges, suggesting that the BrTHF model does not rely excessively on
755 precise tuning of individual inputs. For β , most perturbations lead to minor changes;
756 however, perturbations of $diff_O$ can induce large variability due to the ratio-based nature
757 of β , further highlighting the necessity of the β constraint.

758 To further address potential methodological inconsistencies between buoy-derived
759 fluxes and flux products, we conducted an additional baseline experiment. Specifically,
760 the COARE3.5 model was forced with the same subset of daily meteorological
761 variables used to drive the BrTHF model, thereby providing a method-consistent
762 reference under identical forcing conditions. The results (Table S12) show that the
763 COARE3.5-driven estimates exhibit substantially larger errors for SHF and LHF, with
764 RMSEs of approximately 10.3 W/m^2 and 34.4 W/m^2 , respectively, accompanied by
765 systematic underestimations relative to buoy observations. More importantly,

766 physically unrealistic values of the β emerge in the COARE3.5 estimates, leading to a
767 degradation in β accuracy (RMSE = 6.35). These findings suggest that, even when
768 driven by the same meteorological inputs, traditional bulk formulations remain highly
769 sensitive to forcing uncertainties. In contrast, the BrTHF model demonstrates improved
770 robustness by explicitly incorporating physical constraints within the machine-learning
771 framework.

772 Finally, we examined the potential impact of temporal aggregation, as the buoy-
773 derived daily fluxes used for model training and evaluation were calculated from daily-
774 averaged meteorological variables via COARE3.5, which may introduce biases due to
775 the nonlinearity of bulk flux formulations. By recalculating fluxes from high-frequency
776 buoy observations and aggregating to daily means, we found that although absolute
777 errors differ to some extent, the relative performance among different flux products and
778 models remains unchanged, with the BrTHF model still achieving the best overall
779 accuracy (Table S11). This confirms that our conclusions are robust to the choice of
780 daily flux calculation strategy.

781 3.5.4 Limitations and recommendations

782
783 Although the results demonstrated significant improvements in the accuracy and
784 physical consistency of SHF, LHF, and β estimates from the BrTHF model compared
785 to those from the physics-free NN models and the seven products, the BrTHF product
786 also has some limitations. ~~First, due to the lack of an explicitly defined reasonable range~~
787 ~~for daily β , the constraint of β used in this study was derived from the daily β global~~
788 ~~distribution in the seven widely used global products. While incorporating the~~
789 ~~constraint of β into the model effectively suppresses outliers, it also compresses the~~
790 ~~physically plausible range of β . As a result, the distribution of β shown in Figure 5(i)~~
791 ~~differs notably from other products and models, which may limit the product's~~
792 ~~applicability for users interested in extreme β values. It is highlighted that although the~~
793 ~~BrTHF model slightly underestimates the extreme values of β , it avoids the occurrence~~
794 ~~of unrealistic outliers (e.g., 5 to 500 or -5 to -500) seen in other products, making it~~

795 ~~overall better aligned with observations. Moving forward, we aim to enhance the~~
796 ~~model's ability to preserve physically plausible extremes while maintaining robustness~~
797 ~~against outliers in future updates. First, extreme values of β may arise either from~~
798 ~~physically plausible but rare ocean conditions or from numerical instability or poorly~~
799 ~~constrained estimates associated with uncertainties in model-derived fluxes and input~~
800 ~~variables. In practice, these two sources are difficult to distinguish. To ensure robust~~
801 ~~model training and stable performance across the vast majority of β conditions~~
802 ~~(approximately the 1-99% of the β distribution), we applied a conservative β constraint~~
803 ~~(-5 to 5) during training. This compresses the standard deviation and constrains the~~
804 ~~extreme tails of the predicted β , but substantially improves model stability and accuracy~~
805 ~~for the majority of ocean conditions. Although this choice leads to a narrower dynamic~~
806 ~~range compared to some other products, it ensures that the 1-99% of the β distribution~~
807 ~~is well-represented for most practical applications. It should be noted that this strategy~~
808 ~~represents an interim solution rather than a final one. With future improvements in the~~
809 ~~quality and spatiotemporal representativeness of observational datasets, physically~~
810 ~~plausible extremes (e.g., 0-1% and 99-100% of the β distribution) could be better~~
811 ~~constrained and incorporated into model training, allowing expansion of the dynamic~~
812 ~~range of β .~~ Secondly, the estimated SHF and LHF values exhibited a narrower
813 distribution compared to the observations. This issue possibly stems from the
814 uncertainty of the BrTHF model that was constructed from the uneven distribution of
815 SHF and LHF in the observation datasets, which contain a low proportion of extreme
816 samples, especially negative LHF values. Moreover, due to the insufficient
817 observations, validation and modelling in high-latitude oceans, especially in the
818 Southern Ocean, was limited. To address these problems, more experiments are highly
819 recommended to collect observations covering more regions of oceans with better
820 spatial and temporal representativeness, which could further enhance the product.

821 The BrTHF model demonstrated the feasibility and potential of jointly estimating
822 multiple interrelated air-sea variables through a machine learning model that

823 incorporates appropriate physical constraints to account for their interrelations. In the
824 future, the predicted variables in the BrTHF model could be expanded to include
825 surface radiation, heat storage, and precipitation over the ocean, by integrating the
826 physical mechanisms of energy and water exchange. This would allow for the
827 collaborative optimization of estimates across all components of the air-sea energy and
828 water budgets, potentially contributing to achieving global closure of the air-sea energy
829 and water budgets.

830

831 **4. Data and code availability**

832 The daily 0.25° BrTHF product, consisting of SHF and LHF estimates from 1993
833 to 2017, can be freely accessed from the National Tibetan Plateau Data Center (TPDC)
834 [<https://doi.org/10.11888/Atmos.tpd.c.302578>, Tang and Wang (2025)]. The code for
835 developing the product can be found on the GitHub platform
836 (<https://github.com/zhezhe1996/BrTHF>).

837

838 **5. Summary and Conclusion**

839 In this study, we generated a daily 0.25° air-sea turbulent heat fluxes product for
840 the period from 1993 to 2017 using our developed BrTHF model and multi-source
841 remote sensing and reanalysis data. A comprehensive validation was performed against
842 observations from 197 buoys and inter-comparisons were made with seven
843 representative gridded products. The key findings are as follows:

844 The BrTHF model demonstrated the most significant improvement in estimating
845 the β , while its performance in estimating SHF and LHF was generally comparable to
846 or slightly better than that of the physics-free NN models and the seven widely used
847 air-sea turbulent heat products (including the JOFURO3, IFREMER, SeaFlux, ERA5,
848 MERRA2, OAFflux and OHF products). Through the spatial ten-fold cross-validation
849 against the observations from the 197 buoys, the BrTHF model achieved RMSEs of
850 6.05 W/m² for SHF, 23.67 W/m² for LHF and 0.22 for β , and showed values of r of 0.93,

851 0.91, and 0.25 for SHF, LHF, and β , respectively. Additionally, ~~the~~ BrTHF model
852 performed better in evaluations across six major ocean basins, with lower RMSEs and
853 higher values of r , in comparison to the physics-free NN models and the seven products.
854 Notably, the BrTHF model significantly improved the rationality of β estimates,
855 successfully eliminating the outliers observed in both the physics-free NN models and
856 the seven products. Furthermore, the global distributions for SHF, LHF, and β from the
857 BrTHF product closely matched those of the physically-based ERA5 and SeaFlux
858 products. The global mean annual estimates of SHF, LHF, and β from the BrTHF
859 product from 1993 to 2017 were 12.7 W/m², 106.2 W/m² and 0.11, respectively, all
860 within the ranges of the seven products. The BrTHF product exhibited similar intra-
861 annual cycles for SHF, LHF and β , with bimodal patterns featuring lower and higher
862 peaks in May-June-July-August and December-January, respectively, which was
863 consistent with the results of the seven state-of-the-art products. Additionally, the
864 BrTHF product exhibited significant increasing trends for global SHF and LHF, with
865 rates of 0.04 W/(m² year) and 0.33 W/(m² year), respectively, which were consistent to
866 most of the seven products. In contrast, the BrTHF product displayed weak growth in
867 β , with a trend approaching 0, which ~~were~~was opposite to the results of the seven
868 products except for the MERRA2 product. The increasing (significant increasing)
869 trends dominated the oceans, with areas of 71.4% (26.2%) for SHF, 87.5% (38.9%) for
870 LHF, 53% (12.2%) for β in the BrTHF product.

871 The BrTHF product shows significant advantages in the accuracy and rationality
872 of estimates for key parameters (SHF, LHF, and β) related to air-sea interaction and the
873 global energy and water budgets compared to the existing products. It holds great
874 potential for quantifying the global air-sea energy and water budgets, enhancing our
875 understanding of the air-sea interaction, and projecting climate change under global
876 warming.

877 **Author contribution**

878 YW and RT conceived the study and designed the experimental framework. YW

879 performed the experiment and prepared the initial manuscript draft. All authors
880 contributed to manuscript revision, and approved the final version of the manuscript.

881 **Competing interests**

882 The contact author has declared that none of the authors has any competing
883 interests.

884 **Acknowledgement**

885 We thank the flux datasets and learning datasets provided by the J-OFURO project,
886 IFREMER, ECMWF, NASA, WHOI, NOAA, CEMES and RSS. Moreover, we thank
887 the observations provided by the TAO/TRITON, PIRATA, RAMA, NDBC, TAC, UOP,
888 OOI, AOOS, KOREA, OCS, JKEO and IMO networks or organizations. This work is
889 supported by the National Natural Science Foundation of China [42271378,42071332],
890 and the Strategic Priority Research Program of the Chinese Academy of Sciences
891 (Grant No. XDB0740202).

892

893 **References**

- 894 Bentamy, A., Piollé, J. F., Grouazel, A., Danielson, R., Gulev, S., Paul, F., Azelmat, H.,
895 Mathieu, P. P., von Schuckmann, K., Sathyendranath, S., Evers-King, H., Esau, I.,
896 Johannessen, J. A., Clayson, C. A., Pinker, R. T., Grodsky, S. A., Bourassa, M.,
897 Smith, S. R., Haines, K., Valdivieso, M., Merchant, C. J., Chapron, B., Anderson,
898 A., Hollmann, R., and Josey, S. A.: Review and assessment of latent and sensible
899 heat flux accuracy over the global oceans, *Remote Sensing of Environment*, 201,
900 196-218, 10.1016/j.rse.2017.08.016, 2017.
- 901 Berry, D. I. and Kent, E. C.: Air-Sea fluxes from ICOADS: the construction of a new
902 gridded dataset with uncertainty estimates, *International Journal of Climatology*,
903 31, 987-1001, 10.1002/joc.2059, 2011.
- 904 Bourras, D.: Comparison of five satellite-derived latent heat flux products to moored
905 buoy data, *Journal of Climate*, 19, 6291-6313, 2006.
- 906 Bourras, D., Reverdin, G., Caniaux, G., and Belamari, S.: A Nonlinear Statistical Model
907 of Turbulent Air-Sea Fluxes, *Monthly Weather Review*, 135, 1077-1089,
908 10.1175/mwr3335.1, 2007.
- 909 Bourras, D., Cambra, R., Marié, L., Bouin, M. N., Baggio, L., Branger, H., Beghoura,
910 H., Reverdin, G., Dewitte, B., Paulmier, A., Maes, C., Arduin, F., Pairaud, I.,
911 Fraunié, P., Luneau, C., and Hauser, D.: Air-Sea Turbulent Fluxes From a Wave-

912 Following Platform During Six Experiments at Sea, *Journal of Geophysical*
913 *Research: Oceans*, 124, 4290-4321, 10.1029/2018jc014803, 2019.

914 Bourras, D., Weill, A., Caniaux, G., Eymard, L., Bourlès, B., Letourneur, S., Legain,
915 D., Key, E., Baudin, F., Piguet, B., Traullé, O., Bouhours, G., Sinardet, B., Barrié,
916 J., Vinson, J. P., Boutet, F., Berthod, C., and Cléménçon, A.: Turbulent air-sea
917 fluxes in the Gulf of Guinea during the AMMA experiment, *Journal of*
918 *Geophysical Research: Oceans*, 114, 10.1029/2008jc004951, 2009.

919 Brodeau, L., Barnier, B., Gulev, S. K., and Woods, C.: Climatologically Significant
920 Effects of Some Approximations in the Bulk Parameterizations of Turbulent Air–
921 Sea Fluxes, *Journal of Physical Oceanography*, 47, 5-28, 10.1175/jpo-d-16-0169.1,
922 2017.

923 Brunke, M. A.: Uncertainties in sea surface turbulent flux algorithms and data sets,
924 *Journal of Geophysical Research*, 107, 10.1029/2001jc000992, 2002.

925 Cai, L., Wang, B., Wang, W., and Feng, X.: The Impact of Air–Sea Flux
926 Parameterization Methods on Simulating Storm Surges and Ocean Surface
927 Currents, *Journal of Marine Science and Engineering*, 13, 10.3390/jmse13030541,
928 2025.

929 Chen, X., Yao, Y., Zhao, S., Li, Y., Jia, K., Zhang, X., Shang, K., Xu, J., and Bei, X.:
930 Estimation of High-Resolution Global Monthly Ocean Latent Heat Flux from
931 MODIS SST Product and AMSR-E Data, *Advances in Meteorology*, 2020, 1-19,
932 10.1155/2020/8857618, 2020a.

933 Chen, X., Yao, Y., Li, Y., Zhang, Y., Jia, K., Zhang, X., Shang, K., Yang, J., Bei, X., and
934 Guo, X.: ANN-Based Estimation of Low-Latitude Monthly Ocean Latent Heat
935 Flux by Ensemble Satellite and Reanalysis Products, *Sensors (Basel)*, 20,
936 10.3390/s20174773, 2020b.

937 Clayson, C. and Brown, J.: NOAA Climate Data Record Ocean Surface Bundle (OSB)
938 Climate Data Record (CDR) of Ocean Heat Fluxes, Version 2, *Clim. Algorithm*
939 *Theor. Basis Doc. C-ATBD Asheville NC NOAA Natl. Cent. Environ. Inf. Doi*,
940 10, V59K4885, 2016.

941 Crespo, J., Posselt, D., and Asharaf, S.: CYGNSS Surface Heat Flux Product
942 Development, *Remote Sensing*, 11, 10.3390/rs11192294, 2019.

943 Cummins, D. P., Guemas, V., Cox, C. J., Gallagher, M. R., and Shupe, M. D.: Surface
944 Turbulent Fluxes From the MOSAiC Campaign Predicted by Machine Learning,
945 *Geophysical Research Letters*, 50, 10.1029/2023gl105698, 2023.

946 Cummins, D. P., Guemas, V., Blein, S., Brooks, I. M., Renfrew, I. A., Elvidge, A. D.,
947 and Prytherch, J.: Reducing Parametrization Errors for Polar Surface Turbulent
948 Fluxes Using Machine Learning, *Boundary-Layer Meteorology*, 190,
949 10.1007/s10546-023-00852-8, 2024.

950 Edson, J. B. a. J., Venkata and Weller, Robert A and Bigorre, Sebastien P and
951 Plueddemann, Albert J and Fairall, Christopher W and Miller, Scott D and Mahrt,
952 Larry and Vickers, Dean and Hersbach, Hans: On the Exchange of Momentum
953 over the Open Ocean, *Journal of Physical Oceanography*, 43, 1589-1610,

954 10.1175/jpo-d-12-0173.1, 2013.

955 Fasullo, J. T., Trenberth, K. E., and Balmaseda, M. A.: Earth's Energy Imbalance,
956 *Journal of Climate*, 27, 3129-3144, 10.1175/jcli-d-13-00294.1, 2014.

957 Fu, S., Huang, W., Luo, J., Yang, Z., Fu, H., Luo, Y., and Wang, B.: Deep Learning-
958 Based Sea Surface Roughness Parameterization Scheme Improves Sea Surface
959 Wind Forecast, *Geophysical Research Letters*, 50, 10.1029/2023gl106580, 2023.

960 Gentemann, C. L., Clayson, C. A., Brown, S., Lee, T., Parfitt, R., Farrar, J. T., Bourassa,
961 M., Minnett, P. J., Seo, H., Gille, S. T., and Zlotnicki, V.: FluxSat: Measuring the
962 Ocean–Atmosphere Turbulent Exchange of Heat and Moisture from Space,
963 *Remote Sensing*, 12, 10.3390/rs12111796, 2020.

964 Grist, J. P., Josey, S. A., Zika, J. D., Evans, D. G., and Skliris, N.: Assessing recent air-
965 sea freshwater flux changes using a surface temperature-salinity space framework,
966 *Journal of Geophysical Research: Oceans*, 121, 8787-8806,
967 10.1002/2016jc012091, 2016.

968 Gulev, S. K., Latif, M., Keenlyside, N., Park, W., and Koltermann, K. P.: North Atlantic
969 Ocean control on surface heat flux on multidecadal timescales, *Nature*, 499, 464-
970 467, 10.1038/nature12268, 2013.

971 Jiang, Y., Li, Y., Lu, Y., Wu, T., and Gao, Z.: Evaluating modifications to air–sea
972 momentum flux parameterizations under light wind conditions in CAM6, *Climate
973 Dynamics*, 62, 9687-9701, 10.1007/s00382-024-07415-8, 2024a.

974 Jiang, Y., Li, Y., Lu, Y., Wu, T., Zhang, J., and Gao, Z.: Evaluating nine different air-sea
975 flux algorithms coupled with CAM6, *Atmospheric Research*,
976 10.1016/j.atmosres.2024.107486, 2024b.

977 Jo, Y.-H.: Calculation of the Bowen ratio in the tropical Pacific using sea surface
978 temperature data, *Journal of Geophysical Research*, 107, 10.1029/2001jc001150,
979 2002.

980 Karniadakis, G. E., Kevrekidis, I. G., Lu, L., Perdikaris, P., Wang, S., and Yang, L.:
981 Physics-informed machine learning, *Nature Reviews Physics*, 3, 422-440, 2021.

982 Kashinath, K., Mustafa, M., Albert, A., Wu, J., Jiang, C., Esmaeilzadeh, S.,
983 Azizzadenesheli, K., Wang, R., Chattopadhyay, A., and Singh, A.: Physics-
984 informed machine learning: case studies for weather and climate modelling,
985 *Philosophical Transactions of the Royal Society A*, 379, 20200093, 2021.

986 Kudryavtsev, V., Chapron, B., and Makin, V.: Impact of wind waves on the air-sea
987 fluxes: A coupled model, *Journal of Geophysical Research: Oceans*, 119, 1217-
988 1236, 10.1002/2013jc009412, 2014.

989 Liman, J., Schröder, M., Fennig, K., Andersson, A., and Hollmann, R.: Uncertainty
990 characterization of HOAPS 3.3 latent heat-flux-related parameters, *Atmospheric
991 Measurement Techniques*, 11, 1793-1815, 10.5194/amt-11-1793-2018, 2018.

992 Loeb, N. G., Johnson, G. C., Thorsen, T. J., Lyman, J. M., Rose, F. G., and Kato, S.:
993 Satellite and Ocean Data Reveal Marked Increase in Earth's Heating Rate,
994 *Geophysical Research Letters*, 48, 10.1029/2021GL093047, 2021.

995 Monin, A. S. and Obukhov, A. M.: Basic laws of turbulent mixing in the surface layer

996 of the atmosphere, *Contrib. Geophys. Inst. Acad. Sci. USSR*, 151, e187, 1954.

997 Myslenkov, S., Shestakova, A., and Chechin, D.: The impact of sea waves on turbulent
998 heat fluxes in the Barents Sea according to numerical modeling, *Atmospheric*
999 *Chemistry and Physics*, 21, 5575-5595, 10.5194/acp-21-5575-2021, 2021.

1000 Nelson, J. A., Walther, S., Gans, F., Kraft, B., Weber, U., Novick, K., Buchmann, N.,
1001 Migliavacca, M., Wohlfahrt, G., Šigut, L., Ibrom, A., Papale, D., Göckede, M.,
1002 Duveiller, G., Knohl, A., Hörtnagl, L., Scott, R. L., Zhang, W., Hamdi, Z. M.,
1003 Reichstein, M., Aranda-Barranco, S., Ardö, J., Op de Beeck, M., Billesbach, D.,
1004 Bowling, D., Bracho, R., Brümmer, C., Camps-Valls, G., Chen, S., Cleverly, J. R.,
1005 Desai, A., Dong, G., El-Madany, T. S., Euskirchen, E. S., Feigenwinter, I.,
1006 Galvagno, M., Gerosa, G. A., Gielen, B., Goded, I., Goslee, S., Gough, C. M.,
1007 Heinesch, B., Ichii, K., Jackowicz-Korczynski, M. A., Klosterhalfen, A., Knox, S.,
1008 Kobayashi, H., Kohonen, K.-M., Korkiakoski, M., Mammarella, I., Gharun, M.,
1009 Marzuoli, R., Matamala, R., Metzger, S., Montagnani, L., Nicolini, G., O'Halloran,
1010 T., Ourcival, J.-M., Peichl, M., Pendall, E., Ruiz Reverter, B., Roland, M.,
1011 Sabbatini, S., Sachs, T., Schmidt, M., Schwalm, C. R., Shekhar, A., Silberstein, R.,
1012 Silveira, M. L., Spano, D., Tagesson, T., Tramontana, G., Trotta, C., Turco, F.,
1013 Vesala, T., Vincke, C., Vitale, D., Vivoni, E. R., Wang, Y., Woodgate, W., Yepez,
1014 E. A., Zhang, J., Zona, D., and Jung, M.: X-BASE: the first terrestrial carbon and
1015 water flux products from an extended data-driven scaling framework,
1016 *FLUXCOM-X*, *Biogeosciences*, 21, 5079-5115, 10.5194/bg-21-5079-2024, 2024.

1017 O, S. and Orth, R.: Global soil moisture data derived through machine learning trained
1018 with in-situ measurements, *Sci Data*, 8, 170, 10.1038/s41597-021-00964-1, 2021.

1019 Peng, Z., Tang, R., Jiang, Y., Liu, M., and Li, Z.-L.: Global estimates of 500 m daily
1020 aerodynamic roughness length from MODIS data, *ISPRS Journal of*
1021 *Photogrammetry and Remote Sensing*, 183, 336-351,
1022 10.1016/j.isprsjprs.2021.11.015, 2022.

1023 Robertson, F. R., Roberts, J. B., Bosilovich, M. G., Bentamy, A., Clayson, C. A., Fennig,
1024 K., Schröder, M., Tomita, H., Compo, G. P., Gutenstein, M., Hersbach, H.,
1025 Kobayashi, C., Ricciardulli, L., Sardeshmukh, P., and Slivinski, L. C.:
1026 Uncertainties in Ocean Latent Heat Flux Variations over Recent Decades in
1027 Satellite-Based Estimates and Reduced Observation Reanalyses, *Journal of*
1028 *Climate*, 33, 8415-8437, 10.1175/jcli-d-19-0954.1, 2020.

1029 Shang, K., Yao, Y., Di, Z., Jia, K., Zhang, X., Fisher, J. B., Chen, J., Guo, X., Yang, J.,
1030 Yu, R., Xie, Z., Liu, L., Ning, J., and Zhang, L.: Coupling physical constraints with
1031 machine learning for satellite-derived evapotranspiration of the Tibetan Plateau,
1032 *Remote Sensing of Environment*, 289, 10.1016/j.rse.2023.113519, 2023.

1033 Shie, C.-L., Chiu, L. S., Adler, R., Nelkin, E., Lin, I. I., Xie, P., Wang, F.-C.,
1034 Chokngamwong, R., Olson, W., and Chu, D. A.: A note on reviving the Goddard
1035 Satellite-based Surface Turbulent Fluxes (GSSTF) dataset, *Advances in*
1036 *Atmospheric Sciences*, 26, 1071-1080, 10.1007/s00376-009-8138-z, 2009.

1037 Song, X.: The Importance of Relative Wind Speed in Estimating Air–Sea Turbulent

1038 Heat Fluxes in Bulk Formulas: Examples in the Bohai Sea, *Journal of Atmospheric*
1039 *and Oceanic Technology*, 37, 589-603, 10.1175/jtech-d-19-0091.1, 2020.

1040 Song, X.: The Importance of Including Sea Surface Current when Estimating Air–Sea
1041 Turbulent Heat Fluxes and Wind Stress in the Gulf Stream Region, *Journal of*
1042 *Atmospheric and Oceanic Technology*, 38, 119-138, 10.1175/jtech-d-20-0094.1,
1043 2021.

1044 Song, X., Xie, X., Yan, Y., and Xie, S.-P.: Observed sub-daily variations in air–sea
1045 turbulent heat fluxes under different marine atmospheric boundary layer stability
1046 conditions in the Gulf Stream, *Monthly Weather Review*, 10.1175/mwr-d-24-
1047 0003.1, 2024.

1048 TANG, R. and WANG, Y.: Global dataset of air-sea turbulent heat fluxes (sensible heat
1049 flux and latent heat flux) (1993–2017), National Tibetan Plateau Data Center
1050 [dataset], <https://dx.doi.org/10.11888/Atmos.tpdc.302578>, 2025.

1051 Tang, R., Wang, Y., Jiang, Y., Liu, M., Peng, Z., Hu, Y., Huang, L., and Li, Z.-L.: A
1052 review of global products of air-sea turbulent heat flux: accuracy, mean, variability,
1053 and trend, *Earth-Science Reviews*, 249, 10.1016/j.earscirev.2023.104662, 2024.

1054 Tomita, H., Hihara, T., Kako, S. i., Kubota, M., and Kutsuwada, K.: An introduction to
1055 J-OFURO3, a third-generation Japanese ocean flux data set using remote-sensing
1056 observations, *Journal of Oceanography*, 75, 171-194, 10.1007/s10872-018-0493-
1057 x, 2018.

1058 van der Westhuizen, S., Heuvelink, G. B., and Hofmeyr, D. P.: Multivariate random
1059 forest for digital soil mapping, *Geoderma*, 431, 116365, 2023.

1060 Wang, J., Tang, R., Jiang, Y., Liu, M., and Li, Z.-L.: A practical method for angular
1061 normalization of global MODIS land surface temperature over vegetated surfaces,
1062 *ISPRS Journal of Photogrammetry and Remote Sensing*, 199, 289-304,
1063 10.1016/j.isprsjprs.2023.04.015, 2023.

1064 Wang, W., Chakraborty, T. C., Xiao, W., and Lee, X.: Ocean surface energy balance
1065 allows a constraint on the sensitivity of precipitation to global warming, *Nat*
1066 *Commun*, 12, 2115, 10.1038/s41467-021-22406-7, 2021.

1067 Wang, Y., Tang, R., Huang, L., Liu, M., Jiang, Y., and Li, Z.-L.: A Bowen ratio-informed
1068 method for coordinating the estimates of air–sea turbulent heat fluxes,
1069 *Environmental Research Letters*, 19, 10.1088/1748-9326/ad9341, 2024.

1070 Weller, R. A., Lukas, R., Potemra, J., Plueddemann, A. J., Fairall, C., and Bigorre, S.:
1071 Ocean Reference Stations: Long-Term, Open-Ocean Observations of Surface
1072 Meteorology and Air–Sea Fluxes Are Essential Benchmarks, *Bulletin of the*
1073 *American Meteorological Society*, 103, E1968-E1990, 10.1175/bams-d-21-0084.1,
1074 2022.

1075 Wild, M., Folini, D., Hakuba, M. Z., Schär, C., Seneviratne, S. I., Kato, S., Rutan, D.,
1076 Ammann, C., Wood, E. F., and König-Langlo, G.: The energy balance over land
1077 and oceans: an assessment based on direct observations and CMIP5 climate
1078 models, *Climate Dynamics*, 44, 3393-3429, 10.1007/s00382-014-2430-z, 2014.

1079 Yan, Y., Song, X., Wang, G., and Li, X.: Tropical Cool-Skin and Warm-Layer Effects

1080 and Their Impact on Surface Heat Fluxes, *Journal of Physical Oceanography*, 54,
1081 45-62, 10.1175/jpo-d-23-0103.1, 2024.

1082 Yang, Y., Sun, H., Wang, J., Zhang, W., Zhao, G., Wang, W., Cheng, L., Chen, L., Qin,
1083 H., and Cai, Z.: Global ocean surface heat fluxes revisited: A new dataset from
1084 maximum entropy production framework with heat storage and Bowen ratio
1085 optimizations, *Earth System Science Data Discussions*, 2024, 1-44, 2024.

1086 Yang, Y., Sun, H., Wang, J., Zhang, W., Zhao, G., Wang, W., Cheng, L., Chen, L., Qin,
1087 H., and Cai, Z.: Global ocean surface heat fluxes derived from the maximum
1088 entropy production framework accounting for ocean heat storage and Bowen ratio
1089 adjustments, *Earth System Science Data*, 17, 1191-1216, 10.5194/essd-17-1191-
1090 2025, 2025.

1091 Yu, L.: Global Air–Sea Fluxes of Heat, Fresh Water, and Momentum: Energy Budget
1092 Closure and Unanswered Questions, *Annual Review of Marine Science*, 11, 227-
1093 248, 10.1146/annurev-marine-010816-060704, 2019.

1094 Yu, L. and Weller, R. A.: Objectively Analyzed Air–Sea Heat Fluxes for the Global Ice-
1095 Free Oceans (1981–2005), *Bulletin of the American Meteorological Society*, 88,
1096 527-540, 10.1175/bams-88-4-527, 2007.

1097 Zhang, R., Guo, Weihao, Wang, Xin, and Wang, Chunzai: Ambiguous Variations in
1098 Tropical Latent Heat Flux since the Years around 1998, *Journal of Climate*, 36,
1099 3403–3415, 2023.

1100 Zhao, W. L., Gentine, P., Reichstein, M., Zhang, Y., Zhou, S., Wen, Y., Lin, C., Li, X.,
1101 and Qiu, G. Y.: Physics-Constrained Machine Learning of Evapotranspiration,
1102 *Geophysical Research Letters*, 46, 14496-14507, 10.1029/2019gl085291, 2019.

1103 Zhou, S., Shi, R., Yu, H., Zhang, X., Dai, J., Huang, X., and Xu, F.: A Physical-Informed
1104 Neural Network for Improving Air-Sea Turbulent Heat Flux Parameterization,
1105 *Journal of Geophysical Research: Atmospheres*, 129, 10.1029/2023jd040603,
1106 2024.

1107 Zhou, X., Ray, P., Barrett, B. S., and Hsu, P.-C.: Understanding the bias in surface latent
1108 and sensible heat fluxes in contemporary AGCMs over tropical oceans, *Climate*
1109 *Dynamics*, 55, 2957-2978, 10.1007/s00382-020-05431-y, 2020.

1110